UNIVERSITY OF CALIFORNIA SAN DIEGO

Structural and Dynamical Studies of Condensed Matter Systems Using Advanced Synchrotron Radiation Techniques

A dissertation submitted in partial satisfaction of the
requirements for the degree
Doctor of Philosophy

in

Materials Science and Engineering

by

Jing-Jin Song

Committee in charge:

Professor Sunil K. Sinha, Chair
Professor Richard Averitt
Professor Eric Fullerton
Professor Brian Maple
Professor Oleg Shpyrko

2018

The dissertation of Jing-Jin Song is approved, and it is acceptable in quality and form for publication on microfilm and electronically:

_____

_____

_____

_____

_____

Chair

University of California San Diego

2018

TABLE OF CONTENTS

LIST OF FIGURES

LIST OF TABLES

ACKNOWLEDGEMENTS

First of all, I would like to thank my thesis advisor, Professor Sunil Sinha, for his inspiring guidance and continued support during these past years. I really appreciate that he had offered me the opportunity when I was struggling in finding a place to start my Ph.D. research. He is always kind and encouraging when delivering his knowledge through discussions. He is an excellent example as a wise passionate physicist. To me, he is not only a mentor but also like a father. I have learn much from his serious attitude to science and his wisdom toward life. I believe what he have taught will benefit me in the future no matter where I am.

This thesis work has been done with many collaborators and I want to express my gratitude to all of you. I would like to thank all the scientists at various synchrotron sources, Dr. Cheng Wang, Dr. Suresh Narayanan and Dr. Sujoy Roy, for providing their immense amount of time and knowledge to my research projects. Their supports made the experiments possible. I would also like to thank my collaborators, Dr. Rupak Bhattacharya, Dr. Hongyu Guo, Dr. Sheng Ran, Yi Yang, Tsung-Yeh Tang, Hyunki Kim, Sheena K.K. Patel and Jooyoung Chang for their contributions to the research works. I am grateful to all people who have helped and gave me suggestions during every experiment. I would also like to thank Prof. Brian Maple, Prof. Eric Fullerton, Prof. Oleg Shpyrko and Prof. Richard Averitt for their interest to serve as my thesis committee members.

I gratefully acknowledge the funding source that support my Ph.D. works at UCSD. I was funded by grants from the Division of Basic Energy Science, U.S. Dept. of Energy.

I also want to thank my lab mates, San-Wen Chen, Yicong Ma and Ben Holladay, who make a great group and create a positive working environment.

Finally, I would like to thank my friends and family. My parents always provide me support and have faith in me. I owe them a big and deep thank you.

The text in Chapter 3 is based on material prepared for submission by

R. Bhattacharya, J.-J. Song, C. Wang, G.X. Ni, D. N. Basov, and S. K. Sinha. “Obser-

vation of Two-Dimensional Domain Ordering in Phase Separated Stacked Lipid Bilayers". The dissertation author was the primary investigator and author of this paper.

The text in Chapter 4, in part, is a reprint of the material submitted to Physical Review Letters by

J.-J. Song, R. Bhattacharya, H. Kim; T.-Y. Tang, H. Guo, Y. Yang, J. Chang, H. Kim, S. Narayanan, G. Arya, T. P. Russell, and S. K. Sinha. "One-Dimensional Anomalous Diffusion of Gold Nanoparticles in a Polymer Melt". The dissertation author was the primary investigator and author of this paper.

The content of Chapter 5, is an ongoing project with great help from Sujoy Roy in Lawrence Berkeley National Laboratory. The extension of the work is in collaboration with Prof. Brain Maple, Prof. Eric Fullerton, Dr. Sheng Ran, Dr. Rupak Bhattacharya and Sheena K.K. Patel. The dissertation author was the primary investigator and author.

VITA

2006	B. S. in Materials Science and Engineering *cum laude*, National Tsing Hua University, Hsinchu, Taiwan
2008	M. S. in Materials Science and Engineering, National Tsing Hua University, Hsinchu, Taiwan
2018	Ph. D. in Materials Science and Engineering, University of California, San Diego

ABSTRACT OF THE DISSERTATION

Structural and Dynamical Studies of Condensed Matter Systems Using Advanced Synchrotron Radiation Techniques

by

Jing-Jin Song

Doctor of Philosophy in Materials Science and Engineering

University of California San Diego, 2018

Professor Sunil K. Sinha, Chair

There is the diverse range of disciplines studying various topics using x-ray techniques. Now, with the development of third-generation synchrotron sources, we can conduct experiments which require special properties of x-ray beam, such as coherence and polarization for studying materials characterization, structural changes, molecular or spin dynamics and so on. In this thesis, we would present the results of structural and dynamic studies by synchrotron-produced x-ray sources. First, the lipid phase-separated bilayers are studied by resonant soft x-ray scattering. In the novel finding, we find the domains of the so-called liquid ordered phase in the phase-separated mixed lipid-cholesterol multilayers constitute sub-domains which are three-dimensionally ordered.

This is one of the few examples of ordered liquid phase within another liquid phase. This offers the possibility for the development of novel materials. We also discuss the utilization of coherent x-ray beams to study the dynamics of nanoparticles in polymer melts and magnetic spins in spin glass systems. The nanoparticles show different diffusive and often novel behaviors depending on the entanglement and the heat treatment. Studying the spin structures of spin glass is always interesting and challenging. Up to now, the detailed observation of spin glass phase transition associated critical behaviors have elucidated experimental studies, such as neutron scattering. Using coherent x-rays, we have been able to couple directly to the critical fluctuations of the so-called Edwards-Anderson (EA) order parameter and have observed the dynamical critical behaviors for the first time.

Chapter 1

Introduction

Since German physicist Wilhelm Röntgen discovered and named "x-rays" in 1895, it has been applied in many fields, such as biology, physics, chemistry, etc, with renewed emphasis as higher brilliance synchrotron sources are built worldwide. The use of x-rays is thriving in a wide range of disciplines, because they provide a penetrating probe with wavelengths from 0.1 nm to 10 nm, which are suitable for studying the properties of materials at similar nanometer length scales. The emergence of high-brilliance third- generation synchrotron radiation sources have provided further opportunities to investigate the structures and dynamics of materials in condensed matter physics. Not only the high brilliance, but the tunable properties of synchrotron sources also enable one to get unique information by tuning the energy to various resonance edges of what one is interested in.

This dissertation describes how we applied different x-ray scattering techniques to study the physical properties of various types of condensed matter, including the structure of self-assembled phase-separated lipid multilayers, the diffusion of nanoparticles in polymer melts, and the spin dynamics of a spin glass. This thesis is structured as follows: Chapter 2 includes a brief review of the scientific background of the techniques used in this work. The interaction between x-rays and matter will first be presented. Then small angle x-ray scattering (SAXS) and grazing

incident small angle x-ray scattering (GISAXS) used in the characterization of materials will be introduced. Afterwards, the technique of x-ray photon correlation spectroscopy (XPCS) is also reviewed which can be used in studying the slow dynamics of disordered system. Chapter 3 presents the study of phase-separated lipid stacks from SAXS and GISAXS measurements. The 3-D ordered structure of phase-separated lipid domains has been observed and appears to be independent of the humidity of the surrounding. Chapter 4 covers the study of the anomalous anisotropic diffusive behavior and ballistic motion of gold nanoparticles in a polystyrene (PS) melt. The transition from Brownian motion to anomalous diffusion is shown to be due to the entanglement with the host polymer. Chapter 5 demonstrates the relation between the Edwards-Anderson order parameter and auto-correlation function measured by XPCS in a spin glass system. The transition temperature for freezing magnetic spins is consistent with the divergence of time constant seen in the auto-correlation function. In Chapter 6, the main findings of this work are summarized and the prospective extensions of this work are discussed.

Chapter 2

Experimental Background

The principles involved in this work will be discussed in this chapter. It will begin with the interaction between x-ray photons and matter. Then the different x-ray scattering techniques which were utilized to study the characterization of condensed matter will be covered.

2.1 X-ray Interactions with Matter

The x-ray has been considered as an invaluable tool to probe the structure of matter since it was discovered. The rapid development of synchrotron facilities in the last several decades points to the remarkable explosion of x-ray research. Nowadays, many properties of x-ray have been further used and tailored to meet the requirements of research for different disciplines.

2.1.1 Wave-particle Duality

X-rays are the electromagnetic waves with wavelengths located in the region of one Ångström ($10^{-10}m$) which matches the scale size of atomic spacing. From the concepts in quantum mechanics, x-rays can be treated as photons which carry energy to interact with electrons and the magnetic momentum of electrons in the materials. For a monochromatic x-ray beam, the

numerical relation between the photon energy (E) in keV and wavelength (λ) in Å is given by [1],

$$\lambda[\mathring{A}] = \frac{hc}{E} = \frac{12.398}{E[keV]} \tag{2.1}$$

An x-ray photon interacts with an atom in one of two ways: it can be scattered or it can be absorbed. Here, we will only consider the so-called Thomson scattering [2] (The energy transfer from inelastic scattering is difficult to resolve and negligible in typical experiments using keV x-ray energy). In our studies, we measured the scattering function (S($\mathbf{Q}$)), which is scattering without doing energy analysis of the scattered photons. We will now discuss the scattering with in the classical approximation [3].

2.1.2 Charge Scattering and Scattering Cross-section

We start by considering the most elementary scattering object [4]: an x-ray scattered by a single free electron. In a classical description of the scattering process, the electric field of an incident x-ray beam will force an electron to vibrate and thus radiate the scattered wave. If the incident wave is an electromagnetic plane wave, we can treat the vibrating electron as the source of a spherical wave and the radiated wave (E_{rad}) will depend on the polarization of incident beam (E_{in}). In the far-field limit, the radiated electric filed (modulus squared) at a distance R can be expressed as,

$$|E_{rad}|^2 = |E_{in}|^2 (\frac{r_0^2}{R^2}) P \tag{2.2}$$

where r_0 is referred to as the Thomson Scattering length, or classical radius, of the electron. P, the polarization factor for scattering, depends on the x-ray source. For the synchrotron source, the radiation is usually polarized in the horizontal plane,

$$P = \begin{cases} 1 & \text{vertical scattering plane} \\ \cos^2 2\theta & \text{horizontal scattering plane} \end{cases} \tag{2.3}$$

where 2θ is the total scattering angle projecting in the horizontal plane.

The fundamental quantity determined in a general scattering experiment without energy analysis for the outgoing photons is the differential scattering cross-section ($d\sigma/d\Omega$) which is defined by

$$\frac{d\sigma}{d\Omega} = \frac{\text{No. of X} - \text{ray photons scattered per second into } \Delta\Omega}{\text{Incident flux } \times\ \Delta\Omega} \tag{2.4}$$

where the detector subtends a solid angle $\Delta\Omega$ and the incident flux is given by I_0. I_0 is number of photons incident on the sample per unit area per second. Inserting equation (2.2) into equation (2.4) yields the differential cross section for Thomson scattering from a single electron

$$\frac{d\sigma}{d\Omega} = r_0^2 P \tag{2.5}$$

Now, let us proceed from the scattering by a single electron to consider the case of scattering from one atom with Z electrons. The electron distribution is specified by a number density $\rho(\mathbf{r})$. The scattered radiation field is a superposition of contributions from different elements from the whole volume. The phase difference of scattering from any two locations with a displacement vector $\mathbf{r}$ is

$$\Delta\rho(\mathbf{r}) = (\mathbf{k}_f - \mathbf{k}_0)\cdot\mathbf{r} = \mathbf{Q}\cdot\mathbf{r} \tag{2.6}$$

where $\mathbf{k}_0$ is the incident wavevector and $\mathbf{k}_f$ is the outgoing wavevector. $\mathbf{Q} = \mathbf{k}_f - \mathbf{k}_0$ is known as the wavevector transfer or scattering wavevector. A volume element $d\mathbf{r}$ at $\mathbf{r}$ will contribute an amount $r_0\rho(\mathbf{r})\mathrm{d}\mathbf{r}$ to the scattered field with a phase factor $\mathrm{e}^{i\mathbf{Q}\cdot\mathbf{r}}$. The total scattering length from an atom is thus the Fourier transform of the electron density $\rho(\mathbf{r})$

$$r_0 f^0(\mathbf{Q}) = r_0 \int \rho(\mathbf{r}) e^{i\mathbf{Q}\cdot\mathbf{r}} d\mathbf{r} \tag{2.7}$$

where $f^0(\mathbf{Q})$ is known as the atomic form factor. In the limit of forward scattering that $\mathbf{Q}\rightarrow 0$, all of the different volume elements scatter in phase and yields $f^0(\mathbf{Q}=0)=Z$, the number of electrons in the atom.

The scattering from atomic electrons are of course governed by quantum mechanics. Those electrons have discrete energy levels, and respond to x-ray photons differently, which reduces the scattering length of an atom by some amount. By analogy with a forced harmonic oscillator, the response of the electron will have a phase lag with respect to the driving field. The atomic form factor is now

$$f(\mathbf{Q},\hbar\omega)=f^0(\mathbf{Q})+f'(\hbar\omega)+if''(\hbar\omega) \tag{2.8}$$

where $\hbar\omega$ is the incident x-ray energy. f' and f'' are known as the anomalous corrections to f^0, and they are only significant at x-ray photon energy near an absorption edge.

2.2 Small Angle X-ray Scattering

Small angle x-ray scattering (SAXS), provides detailed physical information and structural analysis for a variety of length scales from 1-100 nm. It is a rapid technique and time-resolved studies based on SAXS yield unique information about kinetics of processes and interactions [5, 6, 7]. Because of the spatial averaging requirement, a SAXS measurement always reduces structural information down to one or two dimensions dependent on the experiment.

2.2.1 General Principles of Small Angle Scattering

In a SAXS experiment, the intensity is expressed as a function of the scattering vector $\mathbf{q}$ resulting from a photon with wavelength λ scattering off the sample at an angle 2θ. The scattering vector is shown as

$$\mathbf{q}=(\mathbf{k}_f-\mathbf{k}_0) \tag{2.9}$$

$$|\mathbf{q}| = \frac{4\pi sin(\theta)}{\lambda} \tag{2.10}$$

The length scale probed in a scattering experiment is of order $2\pi/q$. Therefore in the small angle geometry, the small $\mathbf{q}$ scattering can probe large length scales, instead of the atomic or molecular structures.

The scattering amplitude or form factor, $F(\mathbf{q})$, of an isolated molecule with N atoms for photon energies far from an absorption edge can be determined in an analogous manner to that for a single atom

$$F(\mathbf{q}) = \sum_{i=1}^{N} f_i^0(\mathbf{q}) e^{i\mathbf{q}\cdot\mathbf{r}_i} \tag{2.11}$$

where $\mathbf{r}_i$ is the position of i^{th} atom. The scattered intensity from the isolated molecule is then

$$I(\mathbf{q}) = |F(\mathbf{q})|^2 = \sum_{i=1}^{N}\sum_{j=1}^{N} f_i^0(\mathbf{q}) f_j^0(\mathbf{q}) e^{i\mathbf{q}\cdot(\mathbf{r}_i-\mathbf{r}_j)} \tag{2.12}$$

As x-ray scattering ultimately arise from deviations in electron density from its average, the expression for the scattered intensity then assumes the form

$$I(\mathbf{q}) = f^0(\mathbf{q})^2 \sum_i \int_V [\rho_i(r_{ij}) - \rho_{av}] e^{i\mathbf{q}\cdot(\mathbf{r}_i-\mathbf{r}_j)} dV_j \tag{2.13}$$

where ρ_{av} is the average electron density, and $\rho_i(r_{ij})dV_j$ is the number of atoms or molecules in the volume element dV_j at position $r_j - r_i$ with respect to the reference atom at r_i. The rest of the scatters goes forward to the scattered beam.At small q, one can consider "'smeared out" electron density varying relatively slowly in space, and the small angle scattering intensity can be recast as

$$I^{SAXS}(\mathbf{q}) = f^{0^2} | \int_V (\rho - \rho_{av}) e^{i\mathbf{q}\cdot\mathbf{r}_i} dV_i|^2 \tag{2.14}$$

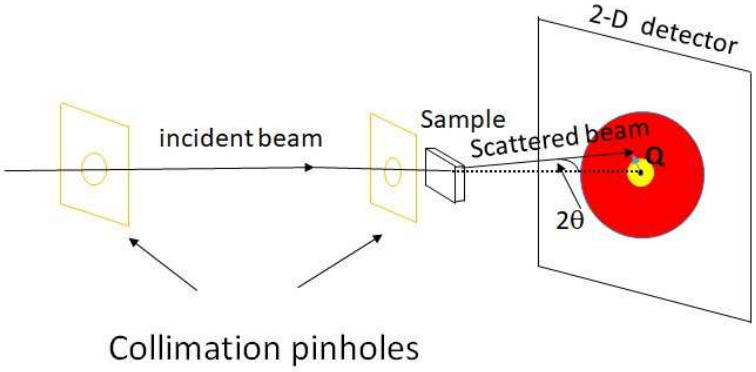

Figure 2.1: Schematic set-up of SAXS.

2.2.2 Typical Experimental Layout

The setup of a SAXS experiment is conceptually simple [8] and shown schematically in Fig 2.1. The x-ray beam first passes through a monochromator to select the x-ray wavelength. Then a series of apertures are used to control the angular divergence. After the collimated x-ray beam impinges on the sample, the intensity of the scattered x-ray is recorded by an x-ray detector [9]. A two-dimensional, position-sensitive detector [10] is invariably used, so that an image is built by each pixel of the detector. It records the number of scattered photons and reflects the intensity as a function of the two components of the wavevector transfer which are nearly perpendicular to the incident beam.

2.3 Grazing Incidence Scattering

When the incident angle is near or below the critical angle of the sample, the x-ray beam is evanescent and penetrates only tens of Ångström into the surface [11]. This makes grazing incidence scattering particularly sensitive to the properties of material at the surface or near the surface.

2.3.1 Refraction and Reflection

The refractive index of a material describes the phase velocity of an electromagnetic wave in the medium. Since the x-ray beam is an electromagnetic wave, the refraction phenomenon is expected between the interfaces between two different media[12]. In general for X-rays, the refractive index can be expressed as

$$n(\mathbf{r},\omega) = 1 - \delta(\mathbf{r},\omega) + i\beta(\mathbf{r},\omega) \tag{2.15}$$

which is slightly smaller than 1 with dispersion and absorption terms

$$\delta(\mathbf{r},\omega) = \frac{\lambda^2}{2\pi} r_0 \sum_i \rho_i(\mathbf{r})\{f_i^0(\mathbf{q}) + f_i'(\omega)\} \tag{2.16}$$

$$\beta(\mathbf{r},\omega) = \frac{\lambda^2}{2\pi} r_0 \sum_i \rho_i(\mathbf{r}) f_i''(\omega) \tag{2.17}$$

If the medium is macroscopically homogeneous, the electron density can be treated as a constant. The refractive index is approximately

$$n \simeq 1 - \frac{\lambda^2 r_0 \rho}{2\pi} + i\frac{\lambda\mu}{4\pi} \tag{2.18}$$

where the μ is the linear absorption coefficient.

Snell's law relates the incident angle α_i to the refracted angle α_t

$$cos(\alpha_i) = ncos(\alpha_t) \tag{2.19}$$

For the x-ray beam, the refractive index smaller than 1 means that below a certain incident angle called the critical angle, α_c, it undergoes total external refection [13]. By taking $\beta = 0$, we can

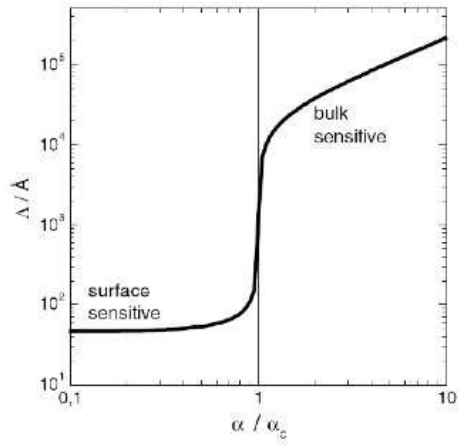

Figure 2.2: Penetration depth changes with normalized incident angle.

relate δ to α_c

$$\alpha_c = \sqrt{2\delta} \tag{2.20}$$

When the total external reflection happens, there is a so-called evanescent wave within the refracting medium. Its amplitude decays rapidly in the materials and propagates parallel to the flat interface. The much-reduced penetration depth of x-rays at angles less than α_c increases their surface sensitivity (shown in Fig 2.2).

2.3.2 Grazing Incident Small Angle X-ray Scattering

The first GISAXS measurement was performed in 1989 by Joanna Levine and Jerry Cohen by using a rotating anode x-ray source [14], and was introduced into the soft matter in 1997 [15]. The typical set-up of GISAXS is presented schematically in Fig 2.3. A collimated x-ray beam is incident on the sample surface at the incident angle near or below the critical angle. The scattered beam from the surface includes the diffuse scattering signals about the specular reflection. Normally, a two-dimensional detector is used to collect the GISAXS data.

The incident angle of GISAXS is typically ≤ 2, so that it includes the surface or interface sensitive information about the sample [16]. The scattered beam will consist of specular

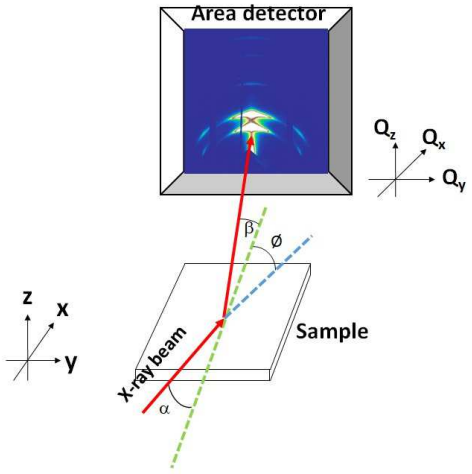

Figure 2.3: Schematic of the typical GISAXS set-up.

reflectivity and off-specular scattering. The specular reflectivity measures the variations in the density normal to the surface, and thus provide characterization of the electron density profile averaged over x-y plane within several naonometers penetration depth. The off-specular scattering, by contrast, measures the variations of scattering density in the x-y plane, which are due to roughness or magnetic domains. For grazing incidence scattering, the x-ray intensity scattered from inhomogeneity at surface, such as surface roughness. It will also be affected by the strong specular reflected wave from the surface, and thus the kinematic approximation is not applied. Instead, the distorted wave Born approximation (DWBA) [17] is developed to account for these dynamical phenomena and to explore the nanostructure of the sample.

2.4 Photon Correlation Spectroscopy

In the last decades, with the development of third generation synchrotron sources, a partially coherent beam of x-ray photons can be obtained. This has opened up a range of new possibilities in x-ray research and technology. Not only for studying the static structure with phase retrieval and speckle reconstruction methods [18], coherent x-rays can also be used to study the slow dynamics of a system through a growing technique known as x-ray photon correlation

spectroscopy (XPCS) [19].

2.4.1 Coherence and Speckles

The coherent properties of light have been examined for hundreds of years. Young's double slit experiment in 1801 demonstrated the interference of coherent light, showing the wave character of the light. However, it was difficult to get a bright coherent light source before the invention of the laser, because one had to throw away almost all of the power by creating the coherent light through a series of pinholes. Techniques, such as dynamical light scattering (DLS), which use coherent visible light to study the structure or dynamics of many systems then expanded enormously because of the invention of the laser.

Compared to visible light source, x-rays have smaller wavelengths and can resolve finer structures. Even so, it is more difficult to obtain coherent x-rays. The typical x-ray beam is not a perfect plane wave and not purely monochromatic. The coherence of a beam of light from an incoherent source is characterized by the coherence lengths

$$l_l = \frac{\lambda}{2}(\frac{\Delta\lambda}{\lambda}) \tag{2.21}$$

$$l_t = \frac{\lambda}{2}(\frac{L}{d}) \tag{2.22}$$

where l_l is the longitudinal coherence length and l_t is the transverse coherence length. L is the distance between the light source and the measuring point, $\Delta\lambda$ is root mean square spread of the incident beam wavelength, and d is the lateral size of the source. Therefore, the coherence volume is proportional to λ^3, which makes the coherence volume of x-rays ten orders smaller than visible light. For a third generation synchrotron source with 0.1 % bandwidth, typical l_l is larger than 1 μm and l_t is located in region between 2 to 150 μm.

The number of photons in the coherence volume is important for experiments with

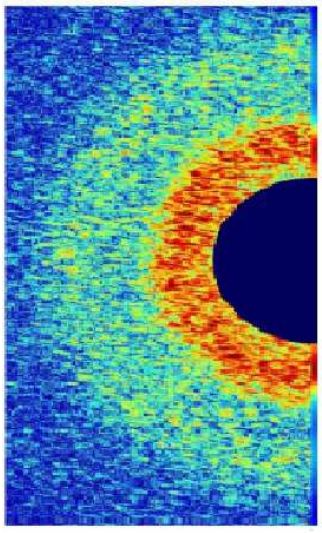

Figure 2.4: A speckle pattern observed by the coherent light.

coherent x-ray beam. The coherent flux depends on the brightness as

$$I_c = \frac{B\lambda^2}{4} \tag{2.23}$$

where B is the number of photons per second per unit source area and unit solid angle. For typical third-generation synchrotron sources, $B > 10^{20}$, making the coherence intensity $I_c > 10^{10}$ photons/second. Unfortunately, the coherence flux decreases with decreasing λ. The higher brilliance is thus necessary for enough intensity for characterizing finer structures.

A speckle pattern [20] (shown as Fig 2.4) is the random intensity pattern observed when the light with sufficient spatial and temporal coherence is scattered by a medium that creates fluctuations of the optical path comparable to the wavelength. In the kinematic approximation, the differential cross section is

$$\frac{d\sigma}{d\Omega}(\mathbf{q}) = r_0^2 P \int\int d\mathbf{r} d\mathbf{r}' < \rho(\mathbf{r})\rho(\mathbf{r}') >_t e^{-i\mathbf{q}\cdot(\mathbf{r}-\mathbf{r}')} \tag{2.24}$$

where the equal-time correlation function is averaged over the time span of the detection. There-

fore, the speckle pattern encodes the exact spatial arrangement of the scattering volume, and it is directly related to the Fourier transform of the sample's electron density. Because of the loss of phase, under normal circumstances it is not possible to recover an image of the electron density by conducting an inverse Fourier transform of the diffraction pattern. However, if a small object is illuminated with coherent radiation, then it becomes possible to retrieve the phases for an inversion by inverting the speckle pattern. (For details, see Refs. [21] [22]).

Any fluctuation in the sample would make a change in the speckle pattern. In the speckle techniques, the coherent volume must be much larger than the length scale of the fluctuation in the sample. The first observation of optical speckles was in 1962 by laser light scattering. Nowadays, the speckle technique is an example of a 'lensless' imaging technique with the benefit of avoiding the need to fabricate complex optical elements. It is widely applied in astronomy, metrology, x-ray scattering, and radar imaging.

2.4.2 X-ray Photon Correlation Spectroscopy

We know the fluctuation in the sample will cause the changes of the speckle pattern, and a measurement of the time-dependence of the intensity of fluctuations of the speckles can reveal the information of the dynamics of this system. The time-dependent variation of the speckles at the reciprocal space vector, $\mathbf{q}$, reflects the dynamical properties at the length scale of $2\pi/q$. The measurement of temporal intensity correlations is the principle of photon correlation spectroscopy (PCS). PCS with visible coherent light is known as Dynamic Light Scattering (DLS) which probes slow dynamics [23, 24, 25] but can cover only the small $\mathbf{q}$ ($< 4 \cdot 10^{-3} \mathring{A}$) regime. XPCS can not only probe much smaller length scales than DLS, but furthermore it obviates multiple scattering, which is a phenomenon frequently complicating the analysis of PCS data in optically opaque systems. Neutron based techniques can access the same q range as XPCS, but probe faster dynamics. Frequency-wave vector space covered by XPCS and its complementary techniques is shown in Fig 2.5 [26].

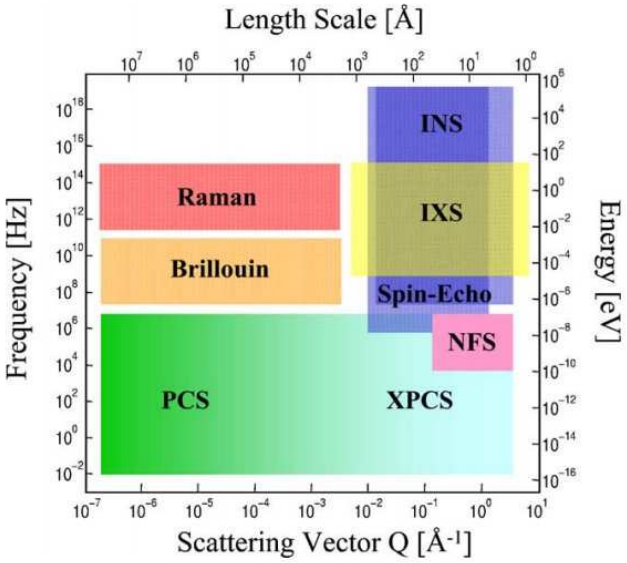

Figure 2.5: Time-scale and Scattering vector (length-scale) covered by x-ray photon correlation spectroscopy and other complementary techniques.

In a typical XPCS experiment, speckle patterns are recorded with an area detector over a constant time interval Δt as the system undergoes dynamics. The temporal correlations can be quantified with the help of the normalized intensity. Then the intensity-intensity autocorrelation function is written as

$$g_2(\mathbf{q},\tau) = \frac{< I(\mathbf{q},t)I(\mathbf{q},t+\tau) >_t}{< I(\mathbf{q},t) >_t^2} \tag{2.25}$$

where the τ is the delay time and $< ... >_t$ is the time average over the whole measurement. The intensity of the scattered beam is proportional to the Fourier transform of the electron density. Assuming the scattered electric fields are random Gaussian variables, then the autocorrelation function will be

$$g_2(\mathbf{q},\tau) = 1 + \beta(\mathbf{q}) \frac{< E(\mathbf{q},t)E^*(\mathbf{q},t+\tau) >_t^2}{< I(\mathbf{q},t) >_t^2} \tag{2.26}$$

where $\beta(\mathbf{q})$ is the contrast parameter of the set-up, it depends on the coherence volume and the illuminated sample volume, as well as the experimental set-up [27, 19]. With perfect coherence, $\beta(\mathbf{q})$ equals to 1. In the actual XPCS measurement, because of the partially coherent beam and

other instrumental imperfections, $\beta << 1$.

The time autocorrelation function $g_2(\mathbf{q},t)$ is frequently expressed in terms of the normalized intermediate scattering function $f(\mathbf{q},t)$ as

$$g_2(\mathbf{q},t) = 1 + \beta(\mathbf{q})|f(\mathbf{q},t)|^2 \tag{2.27}$$

where

$$f(\mathbf{q},t) \propto \int_V \int_V \rho_n(\mathbf{q})\rho_m(\mathbf{q}) e^{-i\mathbf{q}\cdot(\mathbf{r}_n(0)-\mathbf{r}_m(t))} \tag{2.28}$$

$f(\mathbf{q},t)$ is the frequency Fourier transform of the scattering function $S(\mathbf{q},\omega)$measured in an inelastic scattering experiment. The g_2 function can be fitted to a decay function of the form (so-called KWW equation [28]):

$$g_2(\mathbf{q},t) = 1 + \beta(\mathbf{q}) e^{-2(\tau/\tau_0)^\gamma} \tag{2.29}$$

where τ_0 gives the relaxation time constant of the dynamics, and γ is the stretching/compressing exponent.

Bibliography

[1] Carolyn A MacDonald. *An Introduction to X-ray Physics, Optics, and Applications*. Princeton University Press, 2017.

[2] Joseph John Thomson. *Conduction of electricity through gases*. University press, 1903.

[3] Alexander Donnachie and Peter V Landshoff. Elastic scattering and diffraction dissociation. *Nuclear Physics B*, 244(2):322–336, 1984.

[4] Jens Als-Nielsen and Des McMorrow. *Elements of modern X-ray physics*. John Wiley & Sons, 2011.

[5] Luciano Galantini, Claudia Leggio, Peter V Konarev, and Nicolae V Pavel. Human serum albumin binding ibuprofen: a 3d description of the unfolding pathway in urea. *Biophysical chemistry*, 147(3):111–122, 2010.

[6] Masaki Kojima, Masaru Tanokura, Masahiro Maeda, Kazumoto Kimura, Yoshiyuki Amemiya, Hiroshi Kihara, and Kenji Takahashi. ph-dependent unfolding of aspergillopepsin ii studied by small-angle x-ray scattering. *Biochemistry*, 39(6):1364–1372, 2000.

[7] Lois Pollack and Sebastian Doniach. Time-resolved x-ray scattering and rna folding. In *Methods in enzymology*, volume 469, pages 253–268. Elsevier, 2009.

[8] W Bras, GE Derbyshire, AJ Ryan, GR Mant, A Felton, RA Lewis, CJ Hall, and GN Greaves. Simultaneous time resolved saxs and waxs experiments using synchrotron radiation. *Nuclear Instruments and Methods in Physics Research Section A: Accelerators, Spectrometers, Detectors and Associated Equipment*, 326(3):587–591, 1993.

[9] Ch Broennimann, EF Eikenberry, B Henrich, R Horisberger, G Huelsen, E Pohl, B Schmitt, C Schulze-Briese, M Suzuki, T Tomizaki, et al. The pilatus 1m detector. *Journal of synchrotron radiation*, 13(2):120–130, 2006.

[10] B Schmitt, Ch Brönnimann, EF Eikenberry, G Hülsen, H Toyokawa, R Horisberger, F Gozzo, B Patterson, C Schulze-Briese, and T Tomizaki. Development of single photon counting detectors at the swiss light source. *Nuclear Instruments and Methods in Physics Research Section A: Accelerators, Spectrometers, Detectors and Associated Equipment*, 518(1-2):436–439, 2004.

[11] RS Becker, Jene Andrew Golovchenko, and JR Patel. X-ray evanescent-wave absorption and emission. *Physical review letters*, 50(3):153, 1983.

[12] Nanfang Yu, Patrice Genevet, Mikhail A Kats, Francesco Aieta, Jean-Philippe Tetienne, Federico Capasso, and Zeno Gaburro. Light propagation with phase discontinuities: generalized laws of reflection and refraction. *science*, 334(6054):333–337, 2011.

[13] Reginald William James. The optical principles of the diffraction of x-rays. 1954.

[14] Joanne R Levine, JB Cohen, YW Chung, and P Georgopoulos. Grazing-incidence small-angle x-ray scattering: new tool for studying thin film growth. *Journal of Applied Crystallography*, 22(6):528–532, 1989.

[15] Peter Müller-Buschbaum, P Vanhoorne, V Scheumann, and Manfred Stamm. Observation of nano-dewetting structures. *EPL (Europhysics Letters)*, 40(6):655, 1997.

[16] Eric E Fullerton, J Pearson, CH Sowers, SD Bader, XZ Wu, and SK Sinha. Interfacial roughness of sputtered multilayers: Nb/si. *Physical Review B*, 48(23):17432, 1993.

[17] SK Sinha, EB Sirota, Garoff, S, and HB Stanley. X-ray and neutron scattering from rough surfaces. *Physical review B*, 38(4):2297, 1988.

[18] Brian WJ McNeil and Neil R Thompson. X-ray free-electron lasers. *Nature photonics*, 4(12):814, 2010.

[19] D Lumma, LB Lurio, SGJ Mochrie, and M Sutton. Area detector based photon correlation in the regime of short data batches: Data reduction for dynamic x-ray scattering. *Review of Scientific Instruments*, 71(9):3274–3289, 2000.

[20] Sooheyong Lee, W Roseker, C Gutt, B Fischer, H Conrad, F Lehmkühler, I Steinke, D Zhu, H Lemke, M Cammarata, et al. Single shot speckle and coherence analysis of the hard x-ray free electron laser lcls. *Optics express*, 21(21):24647–24664, 2013.

[21] Richard L Sandberg, Ariel Paul, Daisy A Raymondson, Steffen Hädrich, David M Gaudiosi, Jim Holtsnider, I Tobey Raanan, Oren Cohen, Margaret M Murnane, Henry C Kapteyn, et al. Lensless diffractive imaging using tabletop coherent high-harmonic soft-x-ray beams. *Physical review letters*, 99(9):098103, 2007.

[22] JN Cederquist, JR Fienup, JC Marron, and RG Paxman. Phase retrieval from experimental far-field speckle data. *Optics letters*, 13(8):619–621, 1988.

[23] Bruce J Berne and Robert Pecora. *Dynamic light scattering: with applications to chemistry, biology, and physics*. Courier Corporation, 2000.

[24] JC Earnshaw. Surface light scattering: A methodological review, scheduled for publication in the feature issue photon correlation and scattering in applied optics. *Google Scholar*, 1997.

[25] Wyn Brown. *Dynamic light scattering: the method and some applications*, volume 49. Oxford University Press, USA, 1993.

[26] Gerhard Grübel and Federico Zontone. Correlation spectroscopy with coherent x-rays. *Journal of Alloys and Compounds*, 362(1-2):3–11, 2004.

[27] Edward Roy Pike and Herman Z Cummins. *Photon Correlation Spectroscopy and Velocimetry*. Plenum Press, 1977.

[28] Graham Williams and David C Watts. Non-symmetrical dielectric relaxation behaviour arising from a simple empirical decay function. *Transactions of the Faraday society*, 66:80–85, 1970.

Chapter 3

Observation of Two-Dimensional Domain Ordering in Phase Separated Stacked Lipid Bilayers

3.1 Abstract

Liquid-liquid phase separation is emerging as a broad organizing principle across cell biology: It provides a physical-chemical framework to understand the formation of so-called membrane-less organelles inside the cell [1, 2] and that of lipid rafts [3] at the cellular boundaries. In both cases, weak, multivalent interactions dynamically produce local chemical environments that are distinctly different from their global counterparts enabling segregation of molecules and formation of spatial niches for specialized chemistries relevant to the workings of a living cell. Under thermodynamic control, liquid-liquid phase separation in general can be expected to produce complete, macroscopic separation of co-existing phases. But when separation of phases proceed under constraints of reduced dimensionality, anisotropic solvent, and molecularly crowded 'solvents', such as occurs in membranes, a rich phase behavior emerges. Here, we

show that liquid-liquid phase separation, characterizing the formation of cholesterol-enriched, liquid-ordered domains in membrane multilayers, exhibits higher-order structures, hierarchically embedding domains within domains. The ordered distribution of nanoscale domains within the mesoscale domains is reminiscent of the hierarchical ordering, which characterizes complex, cooperative self-assembly processes of mixtures containing nanoparticles [4] and colloids [5], polymers, and even mesoporous zeolites [6]. The interesting hierarchical structure of these systems opens the possibility of synthesizing novel functional materials from liquid-crystalline phases of stacked lipid bilayers.

3.2 Introduction

The phase separation of phospholipid mixtures incorporating cholesterol in lipid membranes has been of considerable interest over the last decade. This was originally driven by the 'raft hypothesis' [3, 7, 8, 9, 10, 11] which proposed the existence of locally structured regions in fluid biological plasma membranes which provide platforms for anchoring of membrane proteins and specific biological functions[12, 11]. The simplified model systems conventionally used to study these effects have generally been bilayers involving mixtures of saturated and unsaturated lipids (such as 1,2-dipalmitoylsn-glycero-3-phosphocholine (DPPC) and 1,2-dioleoyl-sn-glycero-3-phosphocholine (DOPC)) with varying concentrations of cholesterol studied in giant unilamellar vesicles [13, 14] or solid supported films [15, 16, 17, 18], and the ternary phase diagram has been mapped. The phase separation occurs into two coexisting phases, known as the 'Liquid ordered' (L_o) and 'Liquid disordered' (L_d) phases. The cholesterol is predominantly associated with the saturated lipid chains in the L_o phase. GISAXS measurements have shown very short-range ordered lipid molecules within the L_o phase [19], although recent neutron scattering measurements on solid-supported mixtures of cholesterol with single component DPPC lipid bilayers have revealed the existence of highly ordered molecular domains embedded inside the

L_o phase[20]. In solid-supported mixed lipid multilamellar membranes, it has furthermore been shown that the L_o domains register across the bilayers forming columns along the membrane normal threading the L_d phase [15, 21, 22]. The cross-sections of these 'domains' have been imaged using Fluorescence Microscopy [15] and Atomic Force Microscopy [23], and are typically circular in cross-section with diameters $\sim$ 1-2 μm.

3.3 Materials and Methods

3.3.1 Sample Preparation

Phase separated raft phospholipid multilayers were as prepared using 1,2-dioleoyl-sn-glycero-3-phosphocholin (DOPC) and 1,2-dipalmitoyl-sn-glycero-3-phosphocholine (DPPC) in 1:1 ratio with Cholesterol at variable concentrations on silicon [100] substrate by following reported protocol[24, 25]. A concentrated solution (8mg/ml) of desired lipid mixture in chloroform/2,2,2-Trifluroelthanol (1:1) was used to drop coat the films on a freshly cleaned hydrophilic solid substrate. The evaporation rate of the mixed solvent was controlled to obtain a uniform coated film on the substrate over a region of $18mm \times 20mm$. The deposited films were placed in high vacuum overnight to remove trapped solvents. To obtain a well-oriented lipid multilayer, the dried films were rehydrated under 100% relative humidity (RH) at a temperature of 50 °C, well above the gel-fluid transition temperature of the lipid molecules. A slow and steady humidity incubation for more than 48 hours elucidated a well-oriented smectic lipid multilayer membrane with long range correlation among consecutive bilayers. Subsequently, the samples were stored in sealed boxes containing a reservoir of saturated K_2SO_4 salt solution at room temperature and constant RH 98%. During the in-house XRD measurements, we used a specially constructed humidity cell designed for high accuracy and sensitivity in both RH and temperature [26].

3.3.2 Experiments at the Advanced Light Source

Synchrotron x-ray scattering measurements were performed at Advanced Light Source (ALS), Lawrence Berkeley National Laboratory (LBNL) at beamline 11.0.1.2 with monochromatic photon flux 10^{13} photons/s/0.1% BW at 800 eV. A focused beam of dimension $100\mu m \times 100\mu m$ over the desired energy range was employed to get a reasonable scattering signal from the sample. The elliptically polarized undulator (EPU) source provides polarization control for two predefined states i.e with 'S' and 'P' polarizations. The energy of the incident beam can be tuned using a variable-line-space, plane grating monochromator providing soft x-rays in the energy range from 200 to 1500 eV ($\lambda \approx 61.99$ to $8.26\mathring{A}$) and a resolving power of 4000 (at 800 eV). The RSoXS chamber along with the full beam path was operated at high vacuum (10^{-7} Torr) and controlled by LabVIEW interface software developed locally. A customized designed 4-bounce higher order light suppressor was utilized to suppress higher order light harmonics from the EPU and the monochromator.

3.3.3 IR Near-field Scanning Microscopy Imaging

The nano-IR imaging experiments were performed at ambient conditions using a scattering-type scanning near-field microscope (s-SNFM) based on an atomic force microscope (AFM) operating in the tapping mode. A p-polarized mid-IR excitation from a continuous- wave (CW) laser with tunable frequencies was focused on the metallic tip with a radius of 25 nm at the tip apex. A pseudo-heterodyne interferometric detection was used to extract the scattering amplitude and phase of the near-field signal. To remove the IR background, the signal was demodulated at the third harmonic of the tapping frequency 270 kHz.

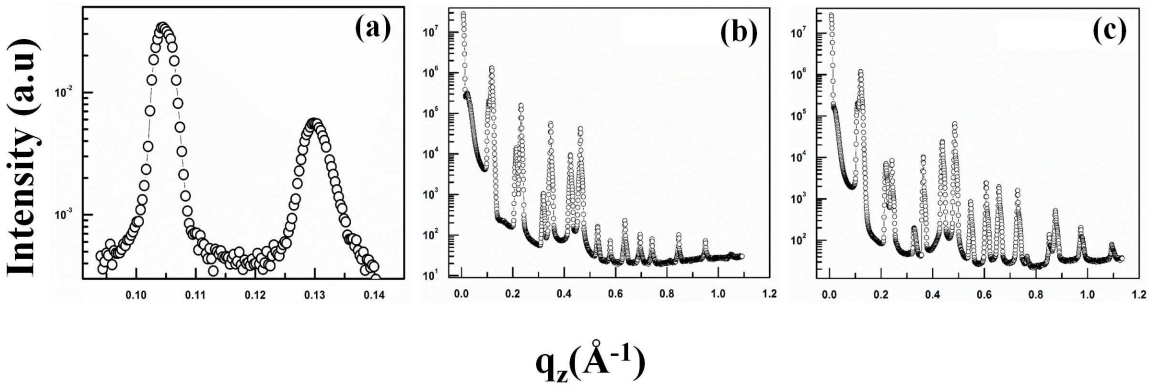

Figure 3.1: (a) XRD profile of multilamellar membrane as a function of q_z at room temperature in presence of ultra-high vacuum($\approx 10^{-7}$ torr) at E $\sim$ 283eV. Similar profiles of the same sample at Cu $K_\alpha(\lambda \sim 1.54Å)$ for (b) 98% humidity & (c) ambient humidity.

3.4 Results and Discussions

In the present study we carried out x-ray diffraction measurements in reflectivity geometry on a multilamellar mixed lipid membrane system consisting of equal amounts of DOPC and DPPC with cholesterol concentrations ranging from 3% to 20%. The membranes were deposited on a silicon single crystal substrate. From the width of the Bragg peaks in the x-ray reflectivity, we estimated the membranes to consist of at least several hundred stacked bilayers. The measurements showed that at room temperature, the membranes were phase separated for all cholesterol concentrations, as shown by two sets of Bragg peaks corresponding to two different bilayer periodicities. The measurements were made in a humidity cell at 98% relative humidity (RH) and in air at ambient RH (see Fig 3.1).

In order to study the lateral structure of the domains, small angle scattering measurements were then carried out in grazing incidence geometry at the Advanced Light Source (ALS) using the Resonant Soft X-Ray Scattering (RSoXS) technique [27, 28], with an x-ray beam of energy tuned near the Carbon K-edge at 283 eV to increase the contrast between the scattering from doubly-bonded C atoms relative to singly-bonded C atoms and other atoms. This serves to increase the scattering contrast between the L_d phase (which is composed primarily of DOPC lipid molecules

which contain C double bonds) and the L_o phase (which contains only the relatively small number of cholesterol molecules possessing double bonds). The measurements were made at room temperature on the phase separated multilamellar membranes, with the samples placed in a high vacuum in the sample chamber of the RSoXS beamline at the ALS.

Remarkably, measurements of the specular Bragg peaks (Fig 3.1) showed that the multilamellar of both phases retained significant amounts of the interlayer water between their head groups, and the periodic multilamellar structure was quite robust in the vacuum. The periodicity of the Lo phase changed by less than 0.2 nm implying relatively little loss of the water between the bilayers, while that of the Ld phase changed by 0.5 nm , implying slightly greater water loss. This robustness of stacked bio-membranes to low ambient humidity has been noticed previously[29]. The grazing angle of incidence of the beam on the sample was 5°. Fig 3.2(A) shows the scattering arrangement, and Fig 3.2(B) shows a typical scattering patterns for a sample containing 20% cholesterol, as imaged by the 2D detector. It shows streaks of diffuse scattering along the intersection of the plane of incidence with the detector plane (the q_z axis) and two pairs of Bragg reflections symmetrically on either side of it.The lower pair of Bragg spots can be understood as arising from cylindrical sub-domains of the L_o phase arranged in a 2D lattice (See Fig 3.4(b)). The q_x, q_y values will be determined by the reciprocal lattice vectors of the 2D lattice. Further, because the x-ray beam sums over many orientations of such lattices in the membrane, the locus of points in reciprocal space from which diffraction can take place is smeared into a ring with constant in-plane wave vector component $q_r = \sqrt{q_x^2 + q_y^2}$ (which was 0.101 $\AA^{-1}$) and at those values of q_z corresponding to the periodicity within these ordered domains along the z-axis, which will be discussed below.

The observed spots on the 2D detector then correspond to the intersection of the Ewald Sphere with these rings, which will lead to symmetrically positioned spots on either side of the vertical q_z axis (See Fig 3.2(A)). The upper pair of spots occur at the same in-plane wave vectors q_r as the lower pair, but with q_z values corresponding to the bilayer periodicity of the ambient L_d

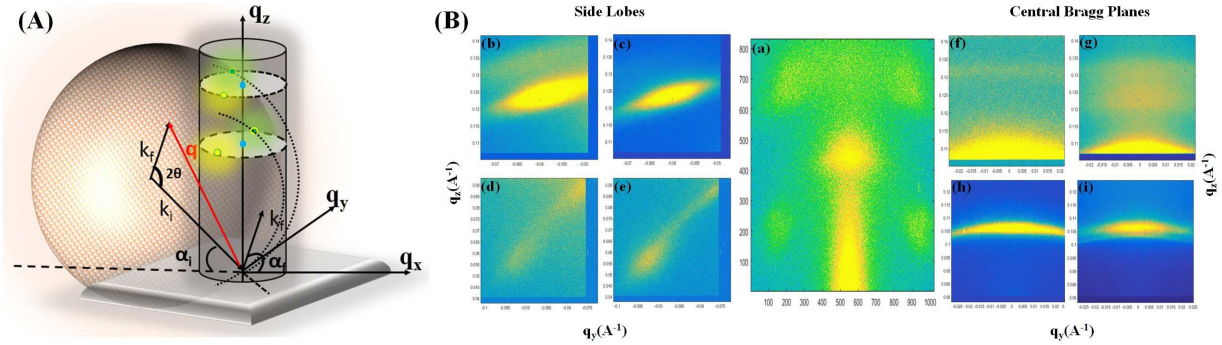

Figure 3.2: (A) The x-ray scattering geometry in reciprocal space. (B) Resonant Soft X-ray Grazing Incidence Small Angle Scattering(GISAXS) pattern at E $\sim$ 283eV from deposited raft membrane on Si[100]. Intensities are presented by false color images. (a) complete detector image in pixels, and in (q_y, q_z)-space with (b) upper side lobe & (c) lower side lobe. Upper central arc for (d) diffuse scattering in the plane of the n=1 Bragg peak for the L_d phase & (e) same for the Bragg plane of the L_o phase.

phase. The appearance of Bragg diffraction from the ambient L_d phase at the same in-plane q value for the ordering of the Lo domains can be understood as an interesting example of Babinet's Principle. These diffraction peaks arise from the negative electron density corresponding to the missing L_d phase within the volumes of the ordered L_o domains. The Bragg reflections from the ordered domains were not visible when the x-ray photon energy was moved off the C=C resonance, indicating insufficient contrast between the two phases at this energy.

The width of the Bragg peaks in the q_y-direction indicated an in-plane size of $\sim$ 100 nm for crystallites of the ordered sub-domains. The q_z value of the Bragg peaks from the in-plane ordering of the L_o domains ($0.055\AA^{-1}$) implies a periodicity along the membrane normal of twice the bilayer periodicity. We speculate that this is due to the ordering of cholesterol domains within the bilayers in every other bilayer, as illustrated in Fig 3.4(a). Ordered cholesterol domains with a different periodicity to the lipid bilayer periodicity have been observed in stacked membranes derived from biological tissue [30]. This type of stacking of the cholesterol domains may arise from the elastic stresses in the lipid layers induced by the binding effects of the cholesterol molecules[16, 31].

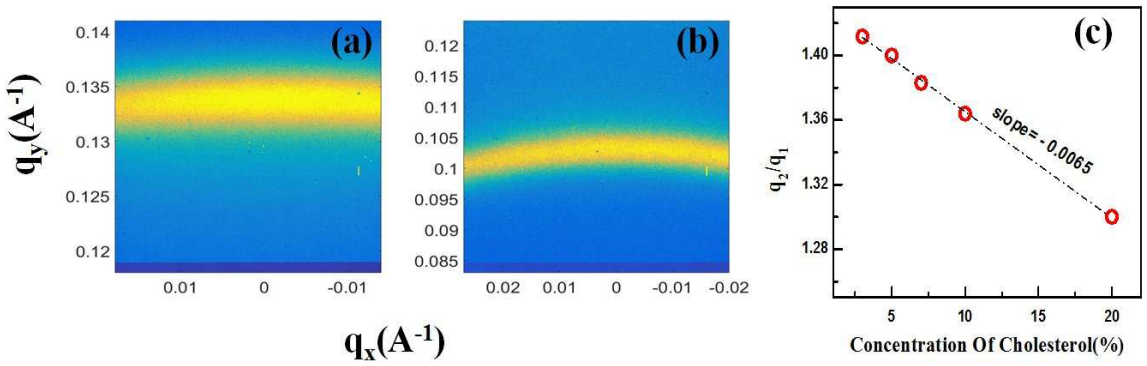

Figure 3.3: Small Angle Resonant Soft X-ray Scattering rings at higher q range for (a) second ring & (b) first ring. (c) Ratio of the q-values of the two rings plotted as a function of cholesterol concentration(%). The black dotted line shows the linear fit over the full concentration range.

In order to obtain more information about the in-plane ordered domain structure, we decided to carry out transmission resonant small angle scattering (RSoXS) experiments at the Carbon double-bond resonant energy with the incident beam normal to the membrane. In order to get a transmitted beam in this case, fresh samples at the same cholesterol concentrations had to be made and deposited on a 100 nm thick SiN membrane. Measurements were again made on samples with the same cholesterol concentrations as in the grazing incidence experiments. We were able to determine two orders of diffraction rings from the ordered domains (see Fig 3.3) and from the ratio of their q values, we were able to conclude that the most probable structure for the ordered domains was an oblique lattice, with a lattice constant equal to 6.2 nm and bond angles close to 90° (distorted square lattice) for the 20% cholesterol sample. On physical grounds, we believe this lattice to be face-centered (see Fig 3.4(b)). The lattice constants and bond angles vary with cholesterol concentration (see Table 3.1).

The appearance of the satellite diffraction peaks to some extent resembles the appearance of satellite peaks in the so-called ripple phases of multilamellar phospholipid films[32]. However, those occur in a single component lipid system and have nothing to do with phase separation, although they might be related to the lateral ordering found here by the system's tendency to

Table 3.1: Parameters obtained from SAXS measurements on phase separated lipid multilayer systems of various Cholesterol concentrations.

% of Cholesterol	$q_r(\AA^{-1})$	q_2/q_1	Nearest neighbor domain spacing(Å)	Bond Angle(°)
3	0.088	1.412	71.36	89.85
5	0.090	1.40	69.78	88.89
7	0.092	1.383	68.26	87.54
10	0.095	1.364	66.10	86.04
20	0.101	1.30	62.17	81.12

develop modulations at these wavelengths.

It is also clear that the ordering we have observed is not the ordering of the lipid molecules in the L_o phase as observed in[20], in which the nearest-neighbor (n.n.) distances are of the order of $5.52\AA$ (corresponding to q_r values too large to explore at the photon wavelengths we used), but instead represent ordering of the L_o domains themselves, as also borne out by the occurrence of a diffraction peak at the identical q_r value (but with a different q_z) from the missing electron density in the ambient L_d phase. We may call the L_o domains which order "sub-domains". Fig 3.4(c) and (d) show nano-infrared (IR) studies of the H_2O bending mode close to its absorption resonance. This is achieved with scanning near-field optical microscopy operating at variable mid-IR laser frequencies[33]. Fig 3.4(c) shows the ratio of near-field amplitude $s(\omega)$ of the scattered field from phase L_d ($s(\omega)_{L_d}$) and L_o ($s(\omega)_{L_o}$) respectively. We found a strong frequency-dependence feature emerge of these two phases. The contrast is strongest at $\omega = 1618 - 1660cm^{-1}$, the frequency that is close to H_2O phonon bending resonance[34] and systematically weakens as the frequency is shifted away from the peak. Fig 3.4(d) shows the real space raster scanned images at $\omega = 1630cm^{-1}$ as an example. Clear domain features from the phase L_o within the phase L_d were observed. The $s(\omega)$ signal from phase L_o is reduced (darker) while enhanced at phase L_d (brighter). This indicates that the H_2O bending mode at these two different phases have distinct IR phonon responses, indicating possible differences in the network of hydrogen-bonded water molecules at the water-headgroup interfaces in the two phases. The 'domains' seen in this and similar images must consist of one or more crystallites of the sub-domains (they are roughly

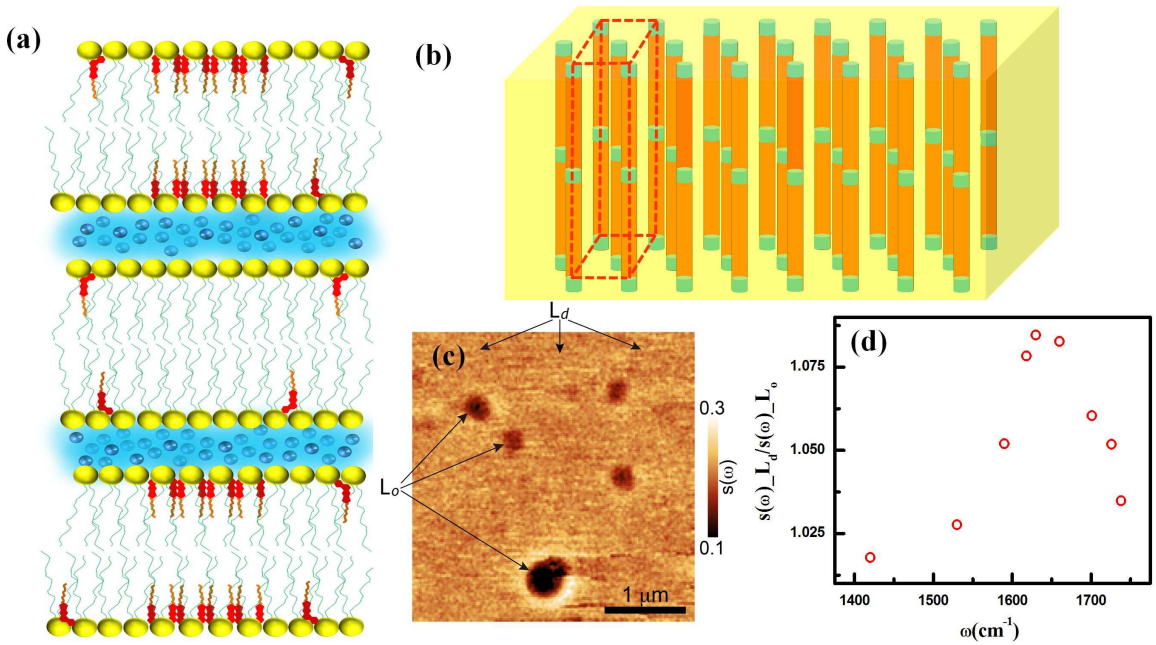

Figure 3.4: (a) Cross section of cholesterol domains inside L_o phase. (b) Schematic shows the face centered oblique structure of crystalline sub-domains of the L_o phase consisting primarily of DPPC & cholesterol. The lipid bilayers of the L_o phase are indicated in orange, and the inter-bilayer water layers are indicated in blue. The unit cell of the ordered sub-domains with twice the bilayer periodicity along the z-axis is denoted by the solid red lines. The surrounding L_d phase is indicated in yellow and its bilayer periodicity is not shown in the figure for reasons of clarity. (c) IR scanning microscope image($\omega = 1630 cm^{-1}$) of a typical phase separated multilayer membrane at 25 °C and ambient humidity. (d) IR intensity ratio spectra as a function of frequencies between L_d and L_o phases.

of the same size, namely $\sim 500nm$ to $1\mu m$). From the images, we conclude that these larger domains have a quasi-random lateral distribution in the membrane with an average n.n. distance of $\approx 1-2\mu m$.

This leads to the question of whether it is the lack of ambient relative humidity (RH) in the x-ray vacuum chamber which causes the domains to order. Currently, there is no way to check if the ordering also occurs under RH values of 98% or greater with RSoXS until a humidity cell planned for the chamber becomes available, although a neutron small angle experiment using a deuterated lipid for contrast is planned for the near future.

3.5 Conclusion

We thus see that the so-called "raft-like" domains in phase separated stacked lipid bilayers with cholesterol are actually hierarchical in structure, with columnar L_o phase sub-domains self-assembling in a local face-centered distorted square lattice and clustering to form domains which are then randomly distributed throughout the membrane. Because the bilayers are periodic along the membrane normal, as in a smectic liquid crystal phase, the sub-domain order is actually 3-dimensional, with a unit cell as shown in Fig 3.4(b). It is likely that these sub-domains are also associated with the highly ordered lipid chains seen in neutron diffraction experiments. Since many external moieties such as proteins (Cholesterol-dependent cytolysin) or functionally treated nanoparticles are known, like cholesterol, to preferentially reside in the L_o domains, this leads to the possibility of creating novel functional materials[35], whose structure is controllable via relative concentration of the components or relative humidity. The fact that these ordered structures which also involve adsorbed inter-lamellar water are stable in high vacuum environments could also lead to novel applications.

This work was supported by a grant from the Bio-molecular Materials Program, Division of Material Science and Engineering, Basic Energy Science, US Department of Energy under

award number DE-SC0018086.

The text in this chapter is based on material prepared for submission by R. Bhattacharya, J.-J. Song, C. Wang, G.X. Ni, D. N. Basov, and S. K. Sinha. “Observation of Two-Dimensional Domain Ordering in Phase Separated Stacked Lipid Bilayers”. The dissertation author was the primary investigator and author of this paper.

Bibliography

[1] Anthony A Hyman and Kai Simons. Beyond oil and waterphase transitions in cells. *Science*, 337(6098):1047–1049, 2012.

[2] Clifford P Brangwynne, Peter Tompa, and Rohit V Pappu. Polymer physics of intracellular phase transitions. *Nature Physics*, 11(11):899–904, 2015.

[3] Daniel Lingwood and Kai Simons. Lipid rafts as a membrane-organizing principle. *science*, 327(5961):46–50, 2010.

[4] Michael A Boles, Michael Engel, and Dmitri V Talapin. Self-assembly of colloidal nanocrystals: From intricate structures to functional materials. *Chemical reviews*, 116(18):11220–11289, 2016.

[5] Prerna Sharma, Andrew Ward, T Gibaud, Michael F Hagan, and Zvonimir Dogic. Hierarchical organization of chiral rafts in colloidal membranes. *Nature*, 513(7516):77, 2014.

[6] Kyungsu Na, Changbum Jo, Jeongnam Kim, Kanghee Cho, Jinhwan Jung, Yongbeom Seo, Robert J Messinger, Bradley F Chmelka, and Ryong Ryoo. Directing zeolite structures into hierarchically nanoporous architectures. *Science*, 333(6040):328–332, 2011.

[7] Kai Simons and Elina Ikonen. Functional rafts in cell membranes. *Nature*, 387(6633):569, 1997.

[8] Maikel C Rheinstädter and Ole G Mouritsen. Small-scale structure in fluid cholesterol–lipid bilayers. *Current opinion in colloid & interface science*, 18(5):440–447, 2013.

[9] Linda J Pike. The challenge of lipid rafts. *Journal of lipid research*, 50(Supplement):S323–S328, 2009.

[10] Pierre-Francois Lenne and Alice Nicolas. Physics puzzles on membrane domains posed by cell biology. *Soft Matter*, 5(15):2841–2848, 2009.

[11] Peter W Janes, Steven C Ley, Anthony I Magee, and Panagiotis S Kabouridis. The role of lipid rafts in t cell antigen receptor (tcr) signalling. In *Seminars in immunology*, volume 12, pages 23–34. Elsevier, 2000.

[12] F Gisou van der Goot and Thomas Harder. Raft membrane domains: from a liquid-ordered membrane phase to a site of pathogen attack. In *Seminars in immunology*, volume 13, pages 89–97. Elsevier, 2001.

[13] Sarah L Veatch and Sarah L Keller. Organization in lipid membranes containing cholesterol. *Physical review letters*, 89(26):268101, 2002.

[14] Peter Heftberger, Benjamin Kollmitzer, Alexander A Rieder, Heinz Amenitsch, and Georg Pabst. In situ determination of structure and fluctuations of coexisting fluid membrane domains. *Biophysical journal*, 108(4):854–862, 2015.

[15] Lobat Tayebi, Yicong Ma, Daryoosh Vashaee, Gang Chen, Sunil K Sinha, and Atul N Parikh. Long-range interlayer alignment of intralayer domains in stacked lipid bilayers. *Nature materials*, 11(12):1074, 2012.

[16] Yicong Ma, Sajal K Ghosh, David A DiLena, Sambhunath Bera, Laurence B Lurio, Atul N Parikh, and Sunil K Sinha. Cholesterol partition and condensing effect in phase-separated ternary mixture lipid multilayers. *Biophysical journal*, 110(6):1355–1366, 2016.

[17] Lin Chen, Zhiwu Yu, and Peter J Quinn. The partition of cholesterol between ordered and fluid bilayers of phosphatidylcholine: a synchrotron x-ray diffraction study. *Biochimica et Biophysica Acta (BBA)-Biomembranes*, 1768(11):2873–2881, 2007.

[18] Pradeep Uppamoochikkal, Stephanie Tristram-Nagle, and John F Nagle. Orientation of tie-lines in the phase diagram of dopc/dppc/cholesterol model biomembranes. *Langmuir*, 26(22):17363–17368, 2010.

[19] Maria K Ratajczak, Eva Y Chi, Shelli L Frey, Kathleen D Cao, Laura M Luther, Ka Yee C Lee, Jaroslaw Majewski, and Kristian Kjaer. Ordered nanoclusters in lipid-cholesterol membranes. *Physical review letters*, 103(2):028103, 2009.

[20] Clare L Armstrong, Drew Marquardt, Hannah Dies, Norbert Kučerka, Zahra Yamani, Thad A Harroun, John Katsaras, An-Chang Shi, and Maikel C Rheinstädter. The observation of highly ordered domains in membranes with cholesterol. *PLoS One*, 8(6):e66162, 2013.

[21] Sanat Karmakar, BR Sarangi, and VA Raghunathan. Phase behaviour of lipid–cholesterol membranes. *Solid state communications*, 139(11-12):630–634, 2006.

[22] Michal Belička, Anna Weitzer, and Georg Pabst. High-resolution structure of coexisting nanoscopic and microscopic lipid domains. *Soft matter*, 13(9):1823–1833, 2017.

[23] Fuyuki Tokumasu, Albert J Jin, Gerald W Feigenson, and James A Dvorak. Nanoscopic lipid domain dynamics revealed by atomic force microscopy. *Biophysical journal*, 84(4):2609–2618, 2003.

[24] M Seul and MJ Sammon. Preparation of surfactant multilayer films on solid substrates by deposition from organic solution. *Thin Solid Films*, 185(2):287–305, 1990.

[25] Xiaoyang Du, JH Whallon, and RI Hollingsworth. Characterization of lipid multilayer microphase structures by phase-contrast and confocal-reflection microscopies. *Langmuir*, 14(19):5581–5585, 1998.

[26] Yicong Ma, Sajal K Ghosh, Sambhunath Bera, Zhang Jiang, Christian M Schlepütz, Evguenia Karapetrova, Laurence B Lurio, and Sunil K Sinha. Anomalous partitioning of water in coexisting liquid phases of lipid multilayers near 100% relative humidity. *Physical Chemistry Chemical Physics*, 18(2):1225–1232, 2016.

[27] E Gann, AT Young, BA Collins, H Yan, J Nasiatka, HA Padmore, H Ade, A Hexemer, and C Wang. Soft x-ray scattering facility at the advanced light source with real-time data processing and analysis. *Review of Scientific Instruments*, 83(4):045110, 2012.

[28] Cheng Wang, Dong Hyun Lee, Alexander Hexemer, Myung Im Kim, Wei Zhao, Hirokazu Hasegawa, Harald Ade, and Thomas P Russell. Defining the nanostructured morphology of triblock copolymers using resonant soft x-ray scattering. *Nano letters*, 11(9):3906–3911, 2011.

[29] Yi Shen, Cyrus R Safinya, Keng S Liang, AF Ruppert, and Kenneth J Rothschild. Stabilization of the membrane protein bacteriorhodopsin to 140 c in two-dimensional films. *Nature*, 366(6450):48, 1993.

[30] R Preston Mason, Thomas N Tulenko, and Robert F Jacob. Direct evidence for cholesterol crystalline domains in biological membranes: role in human pathobiology. *Biochimica et Biophysica Acta (BBA)-Biomembranes*, 1610(2):198–207, 2003.

[31] Wei-Chin Hung, Ming-Tao Lee, Fang-Yu Chen, and Huey W Huang. The condensing effect of cholesterol in lipid bilayers. *Biophysical journal*, 92(11):3960–3967, 2007.

[32] Daniel C Wack and Watt W Webb. Synchrotron x-ray study of the modulated lamellar phase p βin the lecithin-water system. *Physical Review A*, 40(5):2712, 1989.

[33] GX Ni, H Wang, JS Wu, Z Fei, MD Goldflam, F Keilmann, B Özyilmaz, AH Castro Neto, XM Xie, MM Fogler, et al. Plasmons in graphene moiré superlattices. *Nature materials*, 14(12):1217, 2015.

[34] J Paul Devlin, Joanna Sadlej, and Victoria Buch. Infrared spectra of large h2o clusters: New understanding of the elusive bending mode of ice. *The Journal of Physical Chemistry A*, 105(6):974–983, 2001.

[35] D Steer, M Kang, and C Leal. Soft nanostructured films for directing the assembly of functional materials. *Nanotechnology*, 28(14):142001, 2017.

Chapter 4

Observation and Simulation of One-dimensional Anomalous Diffusion of Gold Nanoparticles in a Polymer Melt

4.1 Abstract

We investigated the dynamics of a dilute solution of polymer-chain-grafted gold nanoparticles in polymer melts using x-ray photon correlation spectroscopy. When the host matrix polymer chains are below the molecular weight (MW) for entanglement, normal isotropic diffusion of the gold nanoparticles is observed. If the host polymer chains have a molecular weight above the entanglement molecular weight, anomalous diffusion of the nanoparticles is observed that can be described in terms of ballistic motion and generalized Levy walks, similar to those often used to discuss the dynamics of jammed systems. Further, if the composite samples were initially thermally annealed such that flow could occur, the diffusion is one-dimensional and related to the direction of heat flow during annealing. This unusual behavior is ascribed to an alignment of the host polymer chains in a thermal gradient. Molecular dynamics simulations of a single gold

nanoparticle diffusing in a partially aligned polymer network semiquantitatively reproduce the experimental results to a remarkable degree. The results help to elucidate how nanoparticles can under certain circumstances move rapidly in polymer networks.

4.2 Introduction

Functionalized metal nanoparticles (NPs) inserted in polymers have been of considerable interest recently for several reasons: dilute NPs dispersed in polymers can serve as a unique microrheological probe of the dynamics of the host polymer matrix, while at higher concentrations polymer nanocomposites (PNCs) are formed, which can exhibit a variety of complex thermal, mechanical, rheological, optical and electrical properties[1, 2, 3, 4, 5, 6, 7, 8, 9]. Ensuring effective dispersion of the NPs is one of the key issues in synthesizing PNCs[10]. Consequently, the motion of the functionalized NPs in the embedding matrix is also of intrinsic interest because it reveals how entanglement effects can lead to anomalous diffusion and thus how the NPs disperse at a microscopic level inside the polymer when it is in the melt state, which could be useful in synthesizing PNCs.

4.3 Diffusive Behavior

From several earlier studies, it is known that functionalized nanoparticles introduced into a polymer matrix shows several different regimes of diffusion depending on the degree of entanglement of the chains anchored to the NPs with the host polymer chain. Diffusion ranging from classic Brownian motion to highly anomalous diffusion similar to the motion seen in jammed systems have been observe[11, 12, 13, 14, 15, 16, 17, 18, 19, 20, 21, 22, 23, 24, 25, 26]. For colloidal particles larger than the mesh size or the size of inhomogeneities in the polymer network, the host matrix can be treated as a structureless viscoelastic medium[27], while for NPs much

smaller than the radius of gyration of the polymer chains or adsorbed on the chains, the dynamics seen is the Rouse dynamics of the chain segment[28]. Of particular interest is the regime where the nanoparticle size is comparable to the mesh size, which is the case described here.

For such systems, dynamical measurements may be made using multi-speckle dynamic light scattering (DLS)[11], photoluminescence or fluorescence correlation spectroscopy[12, 13] or its x-ray analog, known as x-ray photon correlation spectroscopy (XPCS)[14, 15, 16, 17, 18, 19, 20, 21, 22, 23, 24]. Such measurements have been carried out on NPs in biopolymers[23], in concentrated polymer solutions[12, 17, 24], and in polymer melts in thin film or bulk form[14, 15, 16, 18, 19, 20, 21, 22]. For NPs in polymer solutions, sub-diffusive behavior has been observed[12, 17]. For polystyrene (PS) melts, Guo et al.[20] found normal hydrodynamic diffusion of Au NPs at high temperatures for host matrices of low to intermediate MW, with the diffusion constant exhibiting a Vogel-Fulcher like behavior as the temperature was decreased, while a crossover to hyper-diffusion with ballistic-like motion occurred as the temperature was lowered to below $\sim 1.1\ T_g$ (glass temperature).

Similar behavior was seen for alumina NPs in PMMA host matrices[19]. This behavior may be attributed to the onset of glassy behavior in the host matrix. Narayanan et al. studied the dynamics of Au NPs in thin films of PS at temperatures well above T_g and observed almost normal diffusion when the host matrix had a MW of 30 Kg/mole but hyper-diffusion with ballistic-like motion for higher MW host PS chains[22]. This behavior may be attributed to entanglement effects with the host matrix.

4.4 XPCS and Dynamics of Nanoparticles

In DLS or XPCS experiments, one measures the normalized scattered intensity autocorrelation function

$$g_2(\mathbf{q},t) = \frac{< I(\mathbf{q},t')I(\mathbf{q},t'+t) >}{< I(\mathbf{q},t') >^2} = 1 + A|f(\mathbf{q},t')|^2 \tag{4.1}$$

where $\mathbf{q}$ ($= 4/\lambda \; sin \; \theta/2$, where θ is the scattering angle and λ is the wavelength of the radiation) is the wave vector transfer, the averages are over time t', A $(0 < A < 1)$ is the instrumental coherence factor (with A= 1 for complete coherence of the beam), and $f(\mathbf{q},t)$ is the normalized intermediate scattering function (ISF) related to the Fourier transform of the scattering function $S(\mathbf{q},\omega)$. Equation (4.1) is based on the assumption of a Gaussian distribution of scattered electric field amplitudes. We assume (to a good approximation) that for NPs with high x-ray contrast, such as gold NPs, the observed scattering represents the dynamics of the NPs alone. For studies of the motion of NPs in polymers, the ISF generally has been fitted with the form

$$f(\mathbf{q},t) = Ce^{(-t/\tau(\mathbf{q}))^{\beta}} \tag{4.2}$$

where for normal diffusion, the exponent $\beta = 1$ and

$$\tau(\mathbf{q}) = \frac{1}{Dq^2} \tag{4.3}$$

where D is the diffusion constant. The hyper-diffusive behavior observed previously for Au NPs in PS melts in certain regimes is usually associated with $\beta > 1$ and

$$\beta(\mathbf{q}) = \frac{1}{Vq} \tag{4.4}$$

where V has the dimensions of a velocity related to a "drift velocity" of the NP as it interacts with the PS chains, acquired due to the release of stresses at random locations in the host matrix, as is believed to occur in jammed systems. If equation (4.4) holds, then Fourier transforming $f(\mathbf{q},t)$ can yield the distribution of particle drift velocities[29], as illustrated below. In several previous studies, β was found to be dependent on both q and temperature, and in some cases $\tau(\mathbf{q})$ was found to crossover between the forms given by Eqs. (4.3) and (4.4) at some values of q[14, 22]. Possible anisotropies in the particle motion have never been explored previously.

In the present work, we report the results of new XPCS studies of functionalized Au NPs dispersed in molten PS which characterize their anomalous diffusion in unprecedented detail, and illustrate several novel features, including anisotropy effects and the effects of stress in the host polymer network. We also present the results of molecular dynamics simulations on systems chosen to represent the samples studied, which agree remarkably well with our experimental results and demonstrate the intermittent random ballistic-like motion predicted by theory. The end result is a clearer picture that emerges of socalled anomalous motion of NPs in an entangled stressed polymer network.

4.5 Experimental Results and Analysis

The volume fraction of the NPs was very small, so as to minimally perturb the host polymer. Two different sizes of Au NPs (13 nm and 18 nm diameter), were densely grafted with ligands of linear PS of MW 38 KDa (g/mole) to prevent aggregation, and dispersed at a volume concentration of 0.5% in host matrices of linear PS of MWs of 13 KDa, 30 KDa and 97 KDa respectively, were studied as a function of temperature. The degree of entanglement of the Au NPs with the host polymer matrix depends on the MW of the ligands relative to the MW of the PS host matrix.

The ligand-grafted NPs were mixed in solution and films were cast, embedding the NPs in the polystyrene matrix. Electron micrographs shown in Fig 4.1, demonstrate that the NPs were well dispersed in the polymer. The mixture was then loaded into a stainless-steel sample container (shown schematically in Fig 4.2) with a circular opening, designed for scattering experiments in a transmission geometry. After the sample was loaded into the cavity, Kapton windows were attached, using Momentive RTV106 high temperature adhesive, to seal the sample. The samples were annealed at 180 ^{0}C in vacuum with the sample cell in the vertical position for more than one day (24 hours) before performing the XPCS measurements. Since the dynamics was dependent

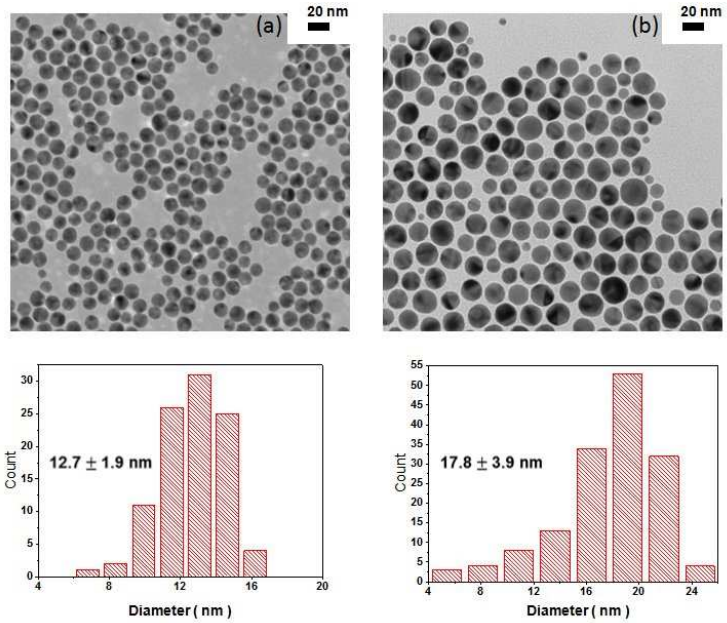

Figure 4.1: Transmission electron microscope (TEM) micrographs of (a) diameter(D): 12.7 $\pm$ 1.9 nm and (b) D: 17.8 $\pm$ 3.9 nm of gold nanoparticles (GNPs), and their particle size distributions.

on the annealing geometry, as will be discussed, we also studied samples annealed with the container in the horizontal position. XPCS experiments were performed at beamline 8-ID-I of the Advanced Photon Source at Argonne National Laboratory using 7.35 keV x-rays. Before the XPCS measurements, small angle x-ray scattering (SAXS) patterns were measured for each sample. The scattering could be described with the squared form factor of the gold nanoparticles, as expected for well-separated gold particles, together with increased scattering at smaller q values. To ensure that the latter was not due to aggregated clusters of the nanoparticles, we verified that the same scattering occurred in a polymer melt without Au NPs, indicating that this was due to large length scale inhomogeneities in the polymer itself.

For most XPCS measurements, the intensity auto-correlation function in equation (4.1) is averaged over all directions of **q** with the same magnitude q, on the assumption of dynamical isotropy, to improve statistical accuracy of counting. In the present experiment however, the pixels in the 2D detector were grouped into 36 pie-shaped sectors, each subtending an angle

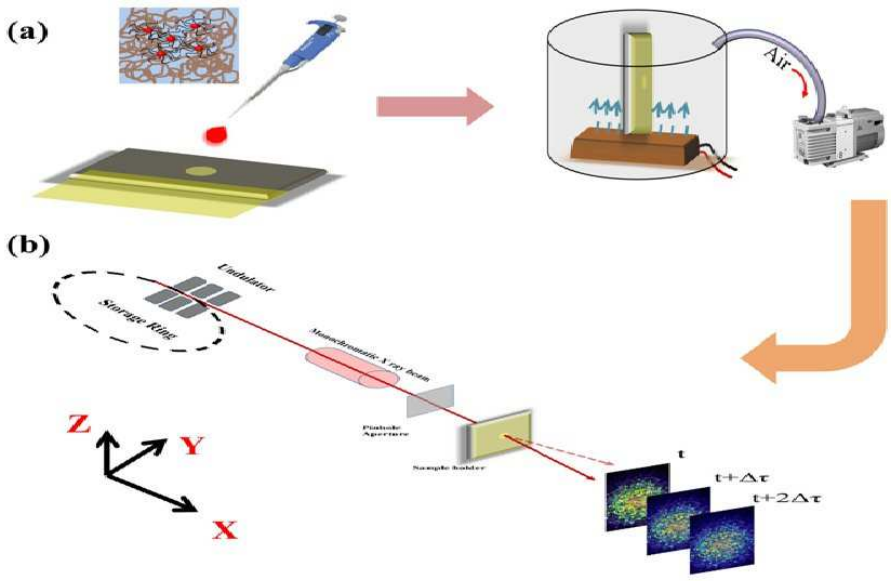

Figure 4.2: (a) Illustration describes the detailed procedure of experiments including loading polymer nanocomposite(PNC) melt into the kapton window sealed sample holder and annealing vertically under high vacuum at temperature higher than the T_g of the sample. (b) Schematic elucidates the X-ray Photon Correlation Spectroscopy (XPCS) beamline setup used for this measurement.

of 100 at the center, and whose mean direction to the vertical is given by the angle ϕ. The g_2 functions defined in equation (4.1) were averaged in each sector over pixels corresponding to a magnitude of q within ranges $\pm\Delta q$, where $\Delta q = 9.6 \times 10^{-4} \mathring{A}^{-1}$. Thus, we measured the functions $g_2(q,\phi,t)$. For some of the samples, surprising oscillatory behavior was observed in time in these functions (see Fig 4.4). An oscillatory g_2 function can arise from uniform convective motion of the nanoparticles, if the scattered beam were heterodyning with some static reference beam[8], e.g. elastic scattering from the sample, but we verified that this was not the case, as for some samples there were no oscillations (as discussed below). The conclusion then is that the oscillations arise from a predominant drift velocity in both directions in the velocity distribution of the particles.

Initially, we discuss only measurements made on samples annealed in the vertical position. These samples show a progression from normal to anomalous diffusion as the chain length of the PS in the host matrix is increased. Fig 4.3(a) shows the functions $(g_2 - 1)$ measured for 18 nm Au

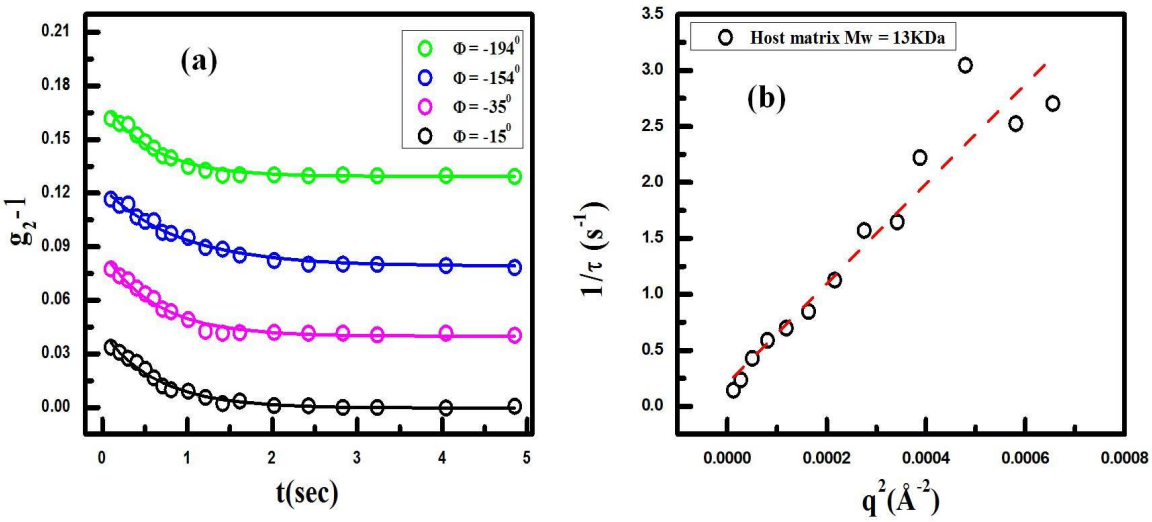

Figure 4.3: (a) $(g_2 - 1)$ as a function of delay time (t) with different ϕs at temperature T = 160°C & $q = 9 \times 10^{-3} \AA^{-1}$ for vertically annealed samples of 18 nm nanoparticles grafted with 38 Kg/mole PS ligands in polymer matrix of MW 13 Kg/mole showing relaxation in terms of (b) Variation of (1/τ) vs g_2 shows pure diffusional motion for the same system.

NPs in the host matrix of MW 13 KDa at 160 ^{0}C for several values of ϕ. These functions showed no dependence on sector angle at any temperature, i.e. were isotropic, and could be described by a single exponential for $f(\mathbf{q},t)$, with relaxation times $\tau \propto q^{-2}$ as expected for normal Brownian motion (see Eqs. (4.2) and (4.3)), yielding a value of D = 445 $\AA^2/sec$ for the diffusion constant at 160 ^0C (see Fig 4.3(b)). This is due to the fact that the PS chains of the host matrix are well below their entanglement MW, so the NPs move without entanglement.

Fig 4.4(a) shows the functions $(g_2 - 1)$ measured for the 18 nm Au NPs in the host matrix of MW 30 KDa at 160 ^0C for $q = 9 \times 10^{-3} \AA^{-1}$ for several different angular sectors. One can see that these functions are oscillatory, but that the period of the oscillation is independent of sector angle ϕ, so that they are functions only of the magnitude of **q**. These functions can be well described, for all q values, sectors and temperatures with the form for $f(\mathbf{q},t)$ given by:

$$f(\mathbf{q},t) = Ae^{-(t/\tau)^{\beta}} \cos(\omega t) \tag{4.5}$$

where β turns out to have a value of ~ 1.8, independent of q and almost temperature independent

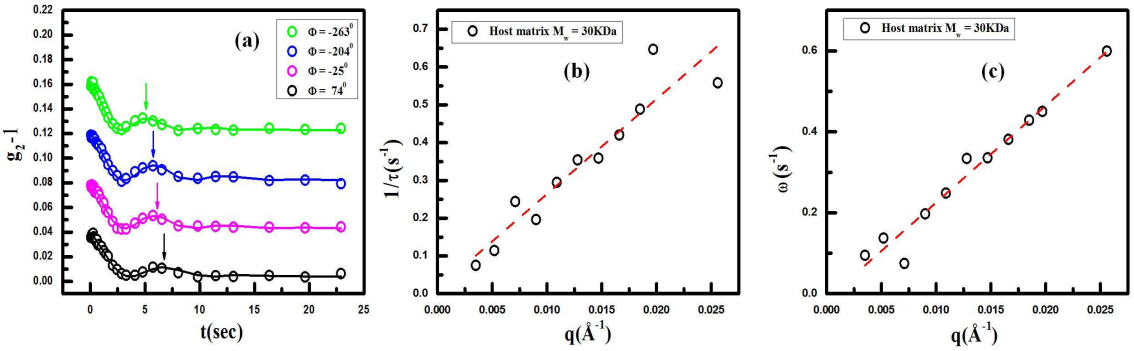

Figure 4.4: (a) Isotropic $(g_2 - 1)$ functions for 18 nm gold particle in host Matrix MW=30 Kg/mole for T = 160°C & $q = 9 \times 10^{-3} \AA^{-1}$. (b) $(1/\tau)$ vs g_2 and (c) ω vs q for the above mentioned system.

(see Table 4.1). $\beta > 1$ indicates that the motion of the nanoparticles are hyper-diffusive. The prefactor A also turned out to be essentially independent of q , temperature and sample and have a value consistent with the instrumental coherence factor, implying that there is no "escape from a cage" at very short timescales[25, 26]. For the above system we find that $\tau = (1/v_1)q^{-1}$ (see equation (4.4)) and $\omega = v_2 q$, where v_1 and v_2 are constants (see Figs 4.4). This corresponds to a ballistic motion of the NPs, with v_1 and v_2 representing two characteristic velocities, that turn out to be dependent on temperature and the size of the NP. Similar results were found for the 13 nm diameter NPs.

$f(\mathbf{q},t)$ is a function only of the single variable qt, which we denote by s, and can be related to the particle velocity distribution P(v) by[29, 30]

$$f(\mathbf{q},t) = f(\mathbf{s}) = \int d\mathbf{v} P(\mathbf{v}) e^{-is\cdot v} \tag{4.6}$$

In the present case, $f(\mathbf{s})$ is isotropic, so that equation (4.6) can be inverted to yield an isotropic velocity distribution P(v), from which the function $W(v)$, the probability of the velocity being

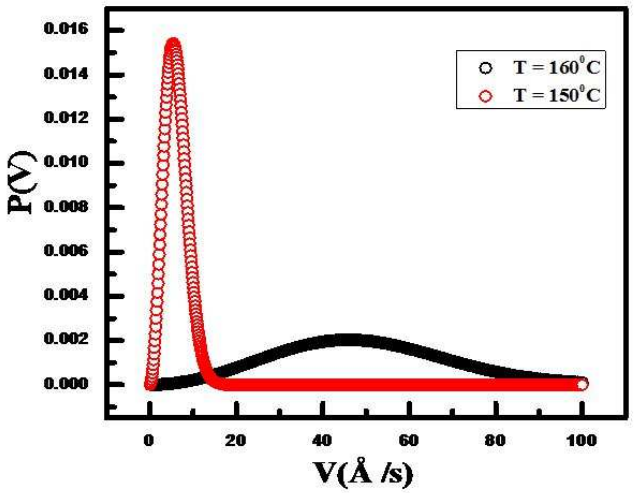

Figure 4.5: Velocity distribution of 18 nm grafted nanoparticle in 30 Kg/mole host matrix at two different temperatures.

between v and (v+dv), can be obtained as:

$$W(v) = 4\pi v^2 P(V) = \frac{2Av}{\pi} \int_0^\infty dsse^{-(v_1 s)^\beta} cos(v_2 s) sin(vs) \tag{4.7}$$

This velocity distribution is shown in Fig 4.5.

Next we present results for the host matrix consisting of chains of MW 97 KDa. The dynamics we observed for this case were strikingly different for samples annealed in the horizontal and in the vertical geometries. For the samples containing 18 nm Au NPs annealed in horizontal geometry, the results are very similar to those reported above for the 30 KDa MW host matrix, with isotropic, oscillatory g_2 functions which can be fit with equation (4.5). For these samples $\beta \simeq 2$, implying a Gaussian spatial self-correlation function for the diffusing particle with a width that increases linearly with time, as expected for ballistic motion

Finally, we discuss the results for samples annealed in vertical geometry in the host matrix of MW 97 KDa. Fig 4.6(a) shows the functions $(g_2 - 1)$ for the 18 nm Au NPs respectively measured at 160 ^0C for $q = 9 \times 10^{-3} \AA^{-1}$ for several different sector angles ϕ. It can be seen that these functions are also oscillatory, but in this case the period of the oscillation varies with ϕ. All

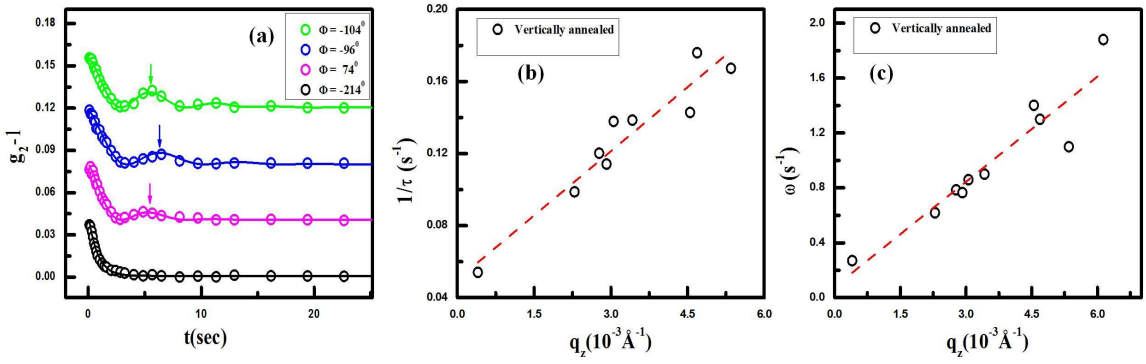

Figure 4.6: (a) Relaxation dynamics in terms of g_2-1 as a function of τ at different angle ϕ at T=160°C and $q = 9 \times 10^{-3} Å^{-1}$ for vertically annealed sample of 97 Kg/mole host matrix with nanoparticle diameter 18 nm. Dependence of (b) $1/\tau$ and (c) ω as a function of $q_z (= qcos\phi)$ at T=160°C for 18nm Au NPs for vertically annealed sample.

these functions can be well fitted for all q values, sector angles ϕ and temperatures, with the form for $f(\mathbf{q},t)$ given by equation (4.5), where $\tau = (1/v_1)(qcos\phi)^{-1}$ and $\omega = v_2 qcos\phi$. (See Figs 4.6). Note that $(qcos\phi)$ is simply q_z the component of **q** in the vertical direction. Thus in this case equation (4.5) may be rewritten as

$$f(\mathbf{q},t) = Ae^{-(v_1 q_z t)^{\beta}} \cos(v_2 q_z t) \tag{4.8}$$

This corresponds to one-dimensional ballistic motion along the q_z axis, with v_1 and v_2 again representing 2 characteristic velocities, which are temperature dependent. Fig 4.7 shows the velocities v_1 and v_2 for the 13nm and 18nm Au NPs as a function of temperature. The function $f(\mathbf{q},t)$ may be inverted by a Fourier transformation with respect to the variable qzt which we denote by s, to yield a one dimensional distribution of particle velocities along the z-axis between v and (v+dv)

$$W(v) = \frac{1}{\sqrt{2\pi}} \int_{-\infty}^{\infty} ds e^{-ivs} e^{-(v_1 s)^{\beta}} cos(v_2 s) = \frac{2}{\sqrt{2\pi}} \int_{0}^{\infty} ds cos(vs) e^{-(v_1 s)^{\beta}} cos(v_2 s) \tag{4.9}$$

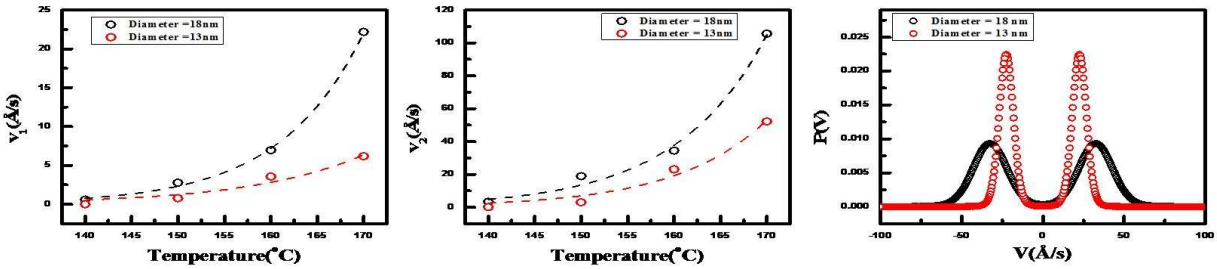

Figure 4.7: The variations of (a) v_1 and (b) v_2 for the 13nm and 18nm Au NPs vertically annealed samples with 97 Kg/mole host matrix as a function of temperature. (c) Velocity distributions at T=160°C.

These velocity distributions are shown in Figs 4.7 for both Au NP diameters. These distributions peak at $v = \pm v_2$ While they resemble, to some extent, the velocity distribution of a damped harmonic oscillator, a calculation of the scattering auto-correlation function $f(\mathbf{q},t)$ from an actual set of independent harmonic oscillators can be shown to yield an expression very different to the form given in equation (4.8). In fact, the dynamics of these samples is ballistic and demonstrate extreme anisotropy, providing an example of drift-like ballistic motion in one dimension. The one-dimensional nanoparticle velocity distributions shown in Fig 4.8 can be represented by a generalized Levy walk[31], characterized by a mean drift velocity (given by v_2), combined with a Levy stable distribution[31, 32, 30] which is given by:

$$L_\mu(z) = \frac{\pi}{2}\int_{-\infty}^{\infty} dk e^{(ikz-|k|^\mu)} \tag{4.10}$$

where $\mu = \beta$, the exponent defined in equation (4.8) and listed in Table 4.1. The velocity distribution corresponds to the Levy stable distributions shifted by $v = \pm v_2$. The theory of such distributions[32] shows that the asymptotic form of the distribution for positive v should go as $(v - v_2)^{-(1+\mu)}$. Fig 4.8 shows that the velocity distribution does indeed asymptotically go as $(v - v_2)^{-(1+\beta)}$. We hypothesize that the one-dimensional motion of the NPs arises from the alignment of the polymer chains of the host matrix during the thermal annealing process, in the vertical geometry along the direction of heat flow, which is confirmed by the molecular dynamics

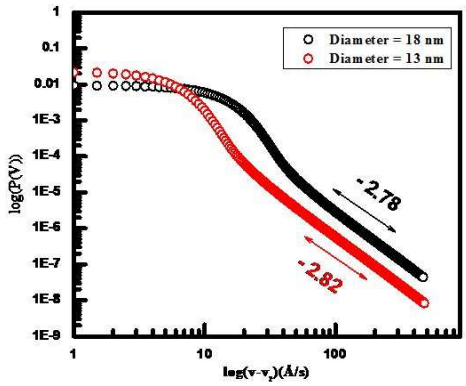

Figure 4.8: $(v - v_2)^{(\mu+1)}$ asymptotic behavior of velocity distribution at 160°C for two different gold nanoparticle sizes. The numbers on the plot indicate the power laws of the two curves.

simulations discussed below.

Table 4.1: Parameters obtained from XPCS fitting of samples with different nanoparticle size, host matrix and annealing conditions at T=160°C.

Annealing condition	Nanoparticle diameter (nm)	Host matrix molecular weight(Kg/mole)	A	β
Vertical	18	13	0.0366±0.0031	1.0
Vertical	18	30	0.0378±0.0014	1.728±0.074
Vertical	13	97	0.0527±0.0043	1.802±0.052
Vertical	18	97	0.0370±0.0025	1.876±0.046
Horizontal	18	97	0.0437±0.0032	1.978±0.055

4.6 Molecular Dynamics Simulations

We conducted molecular dynamics simulations of a single gold NP diffusing in both nonentangled and entangled PS host matrix chains vertically pre-aligned in the z direction. Specifically, the first simulation is comprised of a single PS-grafted NP and short PS chain host matrix (MW $\simeq$ 13 KDa), while the second simulation is comprised of a single PS-grafted NP and long PS chain host matrix (MW $\simeq$ 143 KDa). For the simulations, the polymer chains were initially held aligned along the z-direction and then allowed to relax freely as the NP started

to move. During the simulations, the mean squared displacement (MSD) of the NP and its components along the x-, y-, and z directions were calculated. The MSD is measured over time to determine the nature of the diffusion of the NP and is defined as

$$MSD \equiv < [\mathbf{r}(t) - \mathbf{r}(0)]^2 > \tag{4.11}$$

where $\mathbf{r}(t)$ is the position of the particle at some given time, $\mathbf{r}(0)$ is its reference position, and $< \cdots >$ denotes an average over initial reference positions. We can decompose this into a sum of MSD components along x, y and z respectively. We also calculated the normalized dynamic structure factor $g_1(\mathbf{q},t)$ which is given by

$$g_1(\mathbf{q},t) =< e^{-i\mathbf{q}\cdot\mathbf{r}(0)} e^{i\mathbf{q}\cdot\mathbf{r}(t)} > \tag{4.12}$$

where $q = (2\pi/L)(n_x, n_y, n_z)$; n_x,n_y,n_z are integers, and L is the size of the simulation box. Aside from a constant, the function $g_1(\mathbf{q},t)$ is identical to the normalized intermediate scattering function $f(\mathbf{q},t)$ defined in equation (4.1). We performed calculations of $g_1(\mathbf{q},t)$ with $\mathbf{q}$ along the x,y,z directions (which we label $g_{1,x}$, $g_{1,y}$, and $g_{1,z}$ respectively) with n_x,n_y,n_z ranging from 1 to 6 (Values < 1 correspond to wavelengths incompatible with the periodic boundary conditions).

In the short-chain PS host matrix system, the result of the simulations demonstrates a linear trend of the overall MSD with t and almost equivalent values of the MSD in the x, y and z directions (Fig 4.9(a)) suggesting a normal isotropic diffusive behavior of the NP, as observed experimentally. However, in the higher MW PS host matrix system, the MSD curves are proportional to t^2 over the most of the time scale investigated, which corresponds to ballistic motion (Fig 4.9(b)), although they eventually become linear at much longer times. The x, y components of the MSD are very small, while the z component is almost identical to the total MSD, implying highly anisotropic motion of the NP along the z-direction.

Interestingly, the simulation also shows damped oscillatory behavior of the $g_{1,z}$ curves

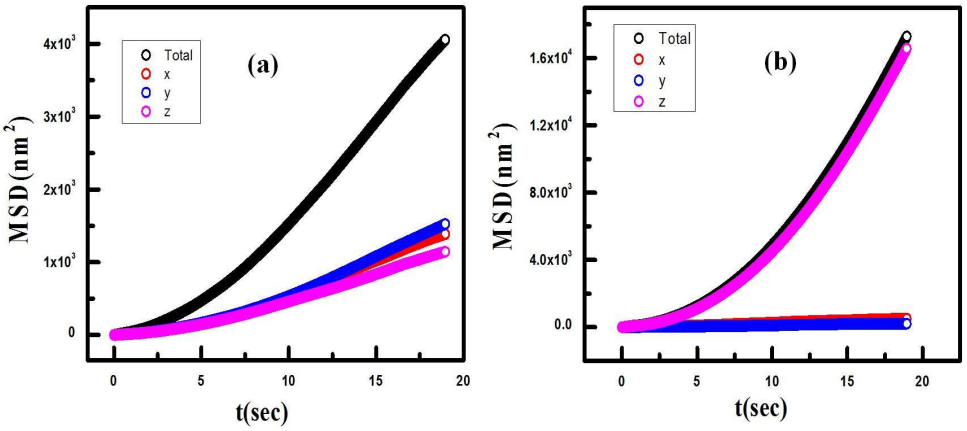

Figure 4.9: (a) Overall mean square displacement(MSD) as a function of time and its x, y, z components of gold NP in $L_m = 7\sigma$ polymer host matrix. (b) Overall mean square displacement(MSD) and its x, y, z components as a function of t(sec) of gold NP in $L_m = 78\sigma$ polymer host matrix.

with time, for different values of q_z, exactly as observed experimentally (Fig 4.10). For instance, we find at q_z $(n_z = 5) = 12.7 \times 10^{-3}\AA^{-1}$, which is close to the experimental value of $q_z = 9 \times 10^{-3}\AA^{-1}$, that the $g_{1,z}$ curve is very consistent with the g_2 curve for $\phi = 104^0$ in terms of the number of oscillations observed, the positions and amplitudes of the oscillations, and the overall range of time scales. Our simulation reveals ballistic motion with velocities $v_{sim} \approx 71\AA/s$ in the same range as the experiments $v_{exp} \approx 38\AA/s$. The reason that v_{sim} is higher than v_{exp} is because the system temperature in the simulations was held fixed at $T \approx 485K$ while it was $T \approx 434K$ in the experiments. Note that because of the exponential dependence of g_1 on the particle position (see equation (4.12)), an oscillatory g_1 does not imply oscillatory motion of the particles, but rather confirms the drift-like motion. However, following the motion of the particle in the simulations did indicate frequent reversals of the direction of motion of the particle. The corresponding $g_{1,xy}$ curves decay without significant oscillation, indicating that the ballistic motion of the NP is confined to the z direction only. It confirms that this anisotropic motion of the NP can be replicated only in the high molecular weight PS host matrix that allows the formation of polymer entanglements. The simulations also show that the motion of the NP

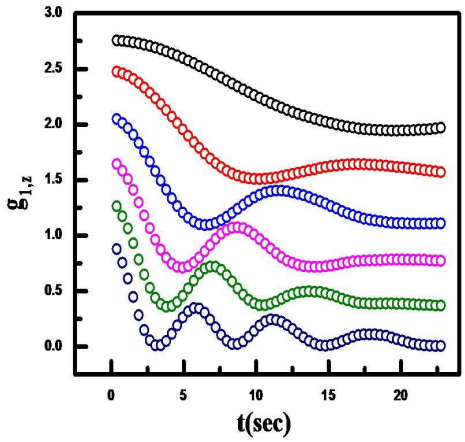

Figure 4.10: $g_{1,z}$ as a function of t(sec) of gold NP in $L_m = 78\sigma$ polymer host matrix. All g_1 curves are normalized and shifted vertically. Here, $q(n) = 2\pi n/(55 \times 45)\mathring{A}^{-1}$.

becomes less anisotropic at longer times. By visualizing the motion of the NP and the polymer chains, we found that the vertical pre-alignment of the PS host matrix chains does not provide permanent constraints. Instead, the PS chains start to slightly coil and relax in all directions immediately after the simulations begin, and eventually allow the NP to also diffuse and interact with polymer entanglements horizontally after a certain given time. Such ageing effects remain to be investigated.

4.7 Conclusions

Previous theoretical treatments[25, 26, 33, 34] and molecular dynamics simulations[35, 36, 37] of NPs moving in polymer networks have yielded either normal Brownian diffusion or sub-diffusion $(MSD \sim t^{\alpha}, \alpha = 1 \; or \; \alpha < 1)$. Ballistic motion has been obtained only for very short times as "escape from the confinement cage"[23, 24], which we do not observe here. Most of the treatments have assumed bare (ungrafted) spherical NPs. To our knowledge, there has been no calculation yielding ballistic hyper-diffusive motion. The theoretical treatment of Bouchaud and Pitard of jammed colloidal particles moving due to the release of elastic stresses in the medium[38] seem more appropriate to the present case. The previously unobserved anisotropic

motion of the NPs seen in the vertically annealed samples in the host matrix of MW = 97 KDa arises from a combination of entanglement effects and the preferential alignment of the PS chains along the long axis of the sample chamber resulting from the heat flow through the sample while it was being annealed in the vertical position, since this anisotropy is not seen in the horizontally annealed samples, where the temperature gradient during annealing is normal to the plane of the sample chamber. This is nicely confirmed by the molecular dynamics simulations. However, as seen previously in other experimental studies, we find that, for host network chains with MW greater than the critical MW for entanglement, even well above the glass transition, the slow, random release of stresses in the network gives rise to drift-like ballistic motion, characterized by $\beta > 1$ and $\tau \sim q^{-1}$ as has been discussed theoretically[38]. We have experimentally characterized the drift velocity distribution and shown that it is governed by a Levy stable distribution around an average drift velocity, which increases with temperature, and interestingly, also with NP diameter, i.e. it can be represented by a generalized Levy walk[31]. It is remarkable that all these phenomena, including the crossover from normal Brownian diffusion for a host matrix consisting of short chain polymers to anomalous anisotropic diffusion with intermediate scattering functions which are oscillatory in time for a long-chain host matrix with aligned chains as seen in the experiments, are semi-quantitatively reproduced by the molecular dynamics simulations reported here. Together, the experimental measurements and simulations provide one of the most detailed descriptions of NPs moving in an entangled polymer network, and show how they are governed by residual stresses in the polymer network, even after considerable annealing.

This work was supported by a grant from the Bio-molecular Materials Program, Division of Material Science and Engineering, Basic Energy Science, US Department of Energy under award number DE-SC0018086.

The text in this chapter, in part, is a reprint of the material submitted to Physical Review Letters by J.-J. Song, R. Bhattacharya, H. Kim; T.-Y. Tang, H. Guo, Y. Yang, J. Chang, H. Kim, S. Narayanan, G. Arya, T. P. Russell, and S. K. Sinha. “One-Dimensional Anomalous Diffusion of

Gold Nanoparticles in a Polymer Melt". The dissertation author was the primary investigator and author of this paper.

Bibliography

[1] Anna C Balazs, Todd Emrick, and Thomas P Russell. Nanoparticle polymer composites: where two small worlds meet. *Science*, 314(5802):1107–1110, 2006.

[2] Russell B Thompson, Valeriy V Ginzburg, Mark W Matsen, and Anna C Balazs. Predicting the mesophases of copolymer-nanoparticle composites. *Science*, 292(5526):2469–2472, 2001.

[3] S Srivastava and JK Basu. Experimental evidence for a new parameter to control the glass transition of confined polymers. *Physical review letters*, 98(16):165701, 2007.

[4] Qiang Zhang and Lynden A Archer. Poly (ethylene oxide)/silica nanocomposites: structure and rheology. *Langmuir*, 18(26):10435–10442, 2002.

[5] SS Sternstein and Ai-Jun Zhu. Reinforcement mechanism of nanofilled polymer melts as elucidated by nonlinear viscoelastic behavior. *Macromolecules*, 35(19):7262–7273, 2002.

[6] Michael E Mackay, Tien T Dao, Anish Tuteja, Derek L Ho, Brooke Van Horn, Ho-Cheol Kim, and Craig J Hawker. Nanoscale effects leading to non-einstein-like decrease in viscosity. *Nature materials*, 2(11):762, 2003.

[7] Giovanni Filippone, Giovanni Romeo, and Domenico Acierno. Viscoelasticity and structure of polystyrene/fumed silica nanocomposites: filler network and hydrodynamic contributions. *Langmuir*, 26(4):2714–2720, 2009.

[8] Hua Wang, Changchun Zeng, Mark Elkovitch, L James Lee, and Kurt W Koelling. Processing and properties of polymeric nano-composites. *Polymer Engineering & Science*, 41(11):2036–2046, 2001.

[9] S Pavlidou and CD Papaspyrides. A review on polymer–layered silicate nanocomposites. *Progress in polymer science*, 33(12):1119–1198, 2008.

[10] Michael E Mackay, Anish Tuteja, Phillip M Duxbury, Craig J Hawker, Brooke Van Horn, Zhibin Guan, Guanghui Chen, and RS Krishnan. General strategies for nanoparticle dispersion. *Science*, 311(5768):1740–1743, 2006.

[11] Luca Cipelletti, Suliana Manley, RC Ball, and DA Weitz. Universal aging features in the restructuring of fractal colloidal gels. *Physical review letters*, 84(10):2275, 2000.

[12] Rami A Omari, Andrew M Aneese, Christopher A Grabowski, and Ashis Mukhopadhyay. Diffusion of nanoparticles in semidilute and entangled polymer solutions. *The Journal of Physical Chemistry B*, 113(25):8449–8452, 2009.

[13] Christopher A Grabowski, Bijoy Adhikary, and Ashis Mukhopadhyay. Dynamics of gold nanoparticles in a polymer melt. *Applied Physics Letters*, 94(2):021903, 2009.

[14] S Srivastava, AK Kandar, JK Basu, MK Mukhopadhyay, LB Lurio, S Narayanan, and SK Sinha. Complex dynamics in polymer nanocomposites. *Physical Review E*, 79(2):021408, 2009.

[15] Daniel Kim, Samanvaya Srivastava, Suresh Narayanan, and Lynden A Archer. Polymer nanocomposites: polymer and particle dynamics. *Soft Matter*, 8(42):10813–10818, 2012.

[16] Anne-Caroline Genix and Julian Oberdisse. Structure and dynamics of polymer nanocomposites studied by x-ray and neutron scattering techniques. *Current Opinion in Colloid & Interface Science*, 20(4):293–303, 2015.

[17] Hongyu Guo, Gilles Bourret, R Bruce Lennox, Mark Sutton, James L Harden, and Robert L Leheny. Entanglement-controlled subdiffusion of nanoparticles within concentrated polymer solutions. *Physical review letters*, 109(5):055901, 2012.

[18] Tadanori Koga, C Li, MK Endoh, J Koo, M Rafailovich, S Narayanan, DR Lee, LB Lurio, and SK Sinha. Reduced viscosity of the free surface in entangled polymer melt films. *Physical review letters*, 104(6):066101, 2010.

[19] R Aravinda Narayanan, P Thiyagarajan, S Lewis, A Bansal, LS Schadler, and LB Lurio. Dynamics and internal stress at the nanoscale related to unique thermomechanical behavior in polymer nanocomposites. *Physical review letters*, 97(7):075505, 2006.

[20] Hongyu Guo, Gilles Bourret, Muriel K Corbierre, Simona Rucareanu, R Bruce Lennox, Khalid Laaziri, Luc Piche, Mark Sutton, James L Harden, and Robert L Leheny. Nanoparticle motion within glassy polymer melts. *Physical review letters*, 102(7):075702, 2009.

[21] Rahul Mangal, Samanvaya Srivastava, Suresh Narayanan, and Lynden A Archer. Size-dependent particle dynamics in entangled polymer nanocomposites. *Langmuir*, 32(2):596–603, 2016.

[22] Suresh Narayanan, Dong Ryeol Lee, Aleta Hagman, Xuefa Li, and Jin Wang. Particle dynamics in polymer-metal nanocomposite thin films on nanometer-length scales. *Physical review letters*, 98(18):185506, 2007.

[23] Aline Grein-Iankovski, Izabel C Riegel-Vidotti, Fernanda F Simas-Tosin, Suresh Narayanan, Robert L Leheny, and Alec R Sandy. Exploring the relationship between nanoscale dynamics and macroscopic rheology in natural polymer gums. *Soft matter*, 12(46):9321–9329, 2016.

[24] A Papagiannopoulos, TA Waigh, A Fluerasu, C Fernyhough, and A Madsen. Microrheology of polymeric solutions using x-ray photon correlation spectroscopy. *Journal of Physics: Condensed Matter*, 17(25):L279, 2005.

[25] Li-Heng Cai, Sergey Panyukov, and Michael Rubinstein. Mobility of nonsticky nanoparticles in polymer liquids. *Macromolecules*, 44(19):7853–7863, 2011.

[26] Li-Heng Cai, Sergey Panyukov, and Michael Rubinstein. Hopping diffusion of nanoparticles in polymer matrices. *Macromolecules*, 48(3):847–862, 2015.

[27] Victor Pryamitsyn and Venkat Ganesan. Origins of linear viscoelastic behavior of polymer-nanoparticle composites. *Macromolecules*, 39(2):844–856, 2006.

[28] Joris Sprakel, Jasper van der Gucht, Martien A Cohen Stuart, and Nicolaas AM Besseling. Rouse dynamics of colloids bound to polymer networks. *Physical review letters*, 99(20):208301, 2007.

[29] BJ Berne and R Pecora. Dynamic light scattering. 1976. *USA, New York*, 2000.

[30] Jean-Philippe Bouchaud and Antoine Georges. Anomalous diffusion in disordered media: statistical mechanisms, models and physical applications. *Physics reports*, 195(4-5):127–293, 1990.

[31] Luca Cipelletti, Laurence Ramos, Suliana Manley, Estelle Pitard, DAVID A Weitz, Eugene E Pashkovski, and Marie Johansson. Universal non-diffusive slow dynamics in aging soft matter. *Faraday Discussions*, 123:237–251, 2003.

[32] V Zaburdaev, S Denisov, and J Klafter. Lévy walks. *Reviews of Modern Physics*, 87(2):483, 2015.

[33] Robert A Riggleman, Gregory Toepperwein, George J Papakonstantopoulos, Jean-Louis Barrat, and Juan J de Pablo. Entanglement network in nanoparticle reinforced polymers. *The Journal of chemical physics*, 130(24):244903, 2009.

[34] Jun Liu, Dapeng Cao, and Liqun Zhang. Molecular dynamics study on nanoparticle diffusion in polymer melts: a test of the stokes- einstein law. *The journal of physical chemistry C*, 112(17):6653–6661, 2008.

[35] F Brochard Wyart and Pierre-Gilles de Gennes. Viscosity at small scales in polymer melts. *The European Physical Journal E*, 1(1):93–97, 2000.

[36] Umi Yamamoto and Kenneth S Schweizer. Theory of nanoparticle diffusion in unentangled and entangled polymer melts. *The Journal of chemical physics*, 135(22):224902, 2011.

[37] Tanya Kairn, Peter J Daivis, Ivan Ivanov, and Sati N Bhattacharya. Molecular-dynamics simulation of model polymer nanocomposite rheology and comparison with experiment. *The Journal of chemical physics*, 123(19):194905, 2005.

[38] J-P Bouchaud and E Pitard. Anomalous dynamical light scattering in soft glassy gels. *The European Physical Journal E*, 6(3):231–236, 2001.

Chapter 5

XPCS Studies of Slow Dynamics of Spin Glass Systems

5.1 Abstract

By using x-ray photon correlation spectroscopy (XPCS), we observed, for the first time, true critical behavior associated with the magnetic spins in the spin glass system (CuMn) approaching the spin glass transition temperature (T_g). In XPCS, the auto-correlation functions are coupled directly to the critical fluctuations of Edwards-Anderson (EA) order parameter. The unique advantages of using of XPCS to study the dynamical behavior are: (1) it could get the information of the non-linear susceptibility correlation, and (2) it can reach the longer time scale (more than thousand seconds) for observing slow freezing of magnetic spins. From the neutron spin echo, the results reflect the rapid spin fluctuations, while the slow fluctuations of the EA order parameter occur at much longer time scales which can only be probed by our XPCS experiments. As the temperature decreases, the time constant we can get from the g_2 function increases dramatically as we approach T_g, implying the transition could be seen by x-ray scattering. The T_g we have extracted from time constants is consistent with the value got from

susceptibility measurements.

5.2 Introduction

The term 'spin glass' was introduced in 1968[1, 2, 3], and the physics of spin glasses is a problem that has received a great deal of attention over the years[4, 5, 6]. The spin glass state refers to a magnetic state of a system in which the interactions between the magnetic moments are "frustrated", i.e. in conflict with each due to disorder so that the spins order in a random non-periodic fashion – they "freeze" into random directions[7]. This is theoretically predicted to occur via a continuous second-order phase transition.Spin-glass behavior is interesting and an intrinsic effect of disorder and competition of the magnetic interactions. A continuous transition to a disordered frozen state represents a novel type of phase transition and researchers have attempted to study this transition and the associated critical behavior without success until now.

Spin-glass properties can be observed in a variety of different systems. A conventional spin glass consists of a random (usually dilute) alloy of magnetic spins in a non-magnetic metal crystal, e.g. Fe in Au or Mn in Cu. Because of the oscillatory nature of the RKKY interaction[8] between the randomly spaced spins via the conduction electrons of the host metal, the magnetic spins see a random exchange field and do not achieve long-range order, but nevertheless freeze in random directions as the temperature is lowered[9]. At the transition temperature T_g at which this occurs, there is a peak in the temperature-dependence of the susceptibility[10, 9, 11]. Below this transition, the configurational average of magnetic spins, $< S_i >$, will be equal to zero, since there is no net magnetization. While on the other hand the configurational average of $< S_i > \cdot < S_i >$ becomes nonzero.

$$Q = \frac{1}{N}\sum_{i=1}^{N} < S_i > \cdot < S_i > \neq 0 \tag{5.1}$$

This quantity, which we can call Q is known as the Edwards-Anderson (EA) order parameter[12] and becomes non-zero as the spins freeze below T_g. It represents the order parameter of the spin

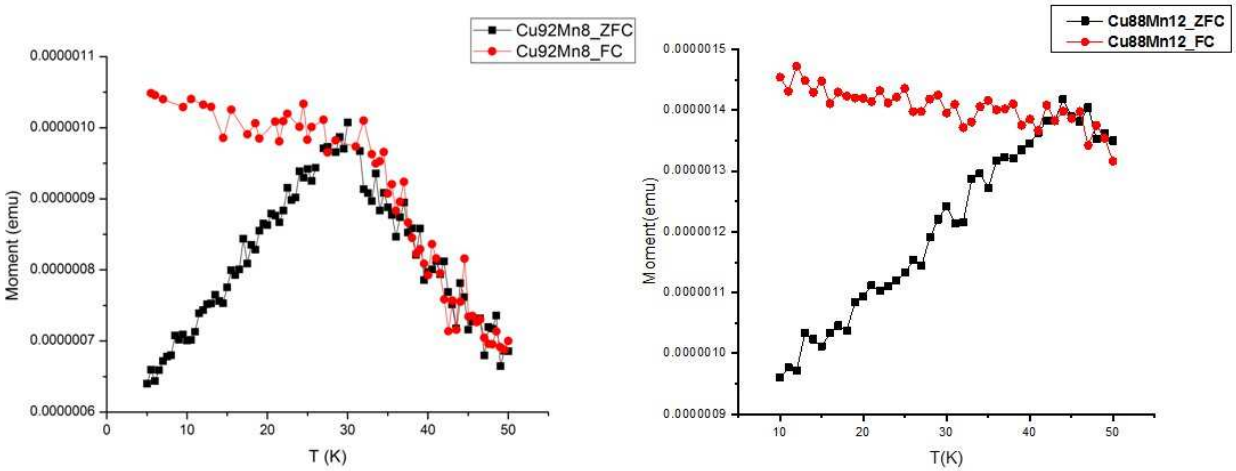

Figure 5.1: DC susceptibilities of CuMn spin glass versus temperature for (a) 8 atom% and (b) 12 atom%

glass state.

5.3 Characteristics of a Spin Glass

We can not identify one sample as a spin glass just by one specific experiment. A system normally should have several properties simultaneously to be classified as a spin glass. One sample may be a spin glass if it poessesses the following defining characteristics: (a) A peak in the temperature-dependent ac-susceptibility at low magnetic fields, occurs around the spin-glass temperature, T_g[13], but it depends on the measuring frequency[14]. (b) A broad peak exists in the temperature-dependence magnetic specific heat[15, 16]. (c) The magnetization measured after zero-field cooling (ZFC) is different from that in field cooling (FC) below the spin glass temperature[17, 18]. (d) Remanence and slow relaxation exist after magnetic perturbation at T_g[19]. (f) No magnetic Bragg peaks would be seen in the neutron diffraction spectrum below T_g, implying no periodic long-range order[20]. (g) In the temperature-dependent dc-susceptibility, T_g can be defined as the intersection point between the measurement after ZFC and that in FC[18](see Fig. 5.1).

5.4 Order Parameter and Auto-correlation Function

In 1975 Edwards and Anderson (EA) revolutionized the statistical mechanics of disordered spin system[12]. They considered the Hamiltonian as

$$\mathcal{H} = -\sum_{i,j} J_{ij} S_i S_j - g\mu_B \mathbf{H} \sum_i S_j \tag{5.2}$$

where J_{ij} is the exchange interaction between spin S_i and spin S_j, H is the external magnetic field, g is the unit magnetic moment, and μ_B is permeability. For $J_{ij} > 0$, the interaction is ferromagnetic, while it will be anti-ferromagnetic coupling as $J_{ij} < 0$

EA also pointed out: Below the "freezing temperature", if one observes a given spin pointing in a certain direction, then there is a finite probability to find the spin pointing in the same direction for a long period of time. Therefore, they proposed the order parameter which describes long-time correlations

$$Q_{EA} = \lim_{t\to\infty} << S_i(t) >< S_i(0) >> \tag{5.3}$$

If this is finite, it can be

$$Q_{EA} = \frac{1}{N} \sum_{i=1}^{N} < S_i > \cdot < S_i > \tag{5.4}$$

which is the same order parameter defined by equation (5.1).

If we consider the magnetic dipole part of the resonant magnetic x-ray cross-section in the quasi-static approximation, it may be written apart from constant factors, as

$$I(\mathbf{q},t) \propto kT\chi(\mathbf{q},t) + N^{-1} \sum_{i,j} < S(t)_i^{\alpha} >< S(t)_j^{\alpha} > e^{-i\mathbf{q}\cdot(\mathbf{r}_i - \mathbf{r}_j)} \tag{5.5}$$

where N is the total number of spins, and $\chi(\mathbf{q},t)$ is the generalized susceptibility defined by

$$kT\chi(\mathbf{q},t) = N^{-1}\sum_{i,j}\{< S(t)_i^{\alpha}S(t)_j^{\alpha} > - < S(t)_i^{\alpha} >< S(t)_j^{\alpha} >\}e^{-i\mathbf{q}\cdot(\mathbf{r}_i-\mathbf{r}_j)} \tag{5.6}$$

Here α denotes the component parallel to the vector $(\mathbf{e}_i \times \mathbf{e}_f)$ where $\mathbf{e}_i$, $\mathbf{e}_f$ are the incident and outgoing photon polarizations. In Eqs. (5.5) and (5.6), the correlation functions refer to equal-time correlation functions at the measurement time t. Equation (5.5) may be written as

$$I(\mathbf{q},t) = kT\chi(\mathbf{q},t) + Q(\mathbf{q},t) \tag{5.7}$$

where Q($\mathbf{q}$,t) is the q-dependent generalization of the EA order parameter to take into account short-range correlations between frozen spins (which are neglected in the simplest formulations).

XPCS measures the quantity[14]

$$g_2(\mathbf{q},t) = \frac{< I(\mathbf{q},0)I(\mathbf{q},t) >}{< I(\mathbf{q},0) >^2} \tag{5.8}$$

where $t = 0$ corresponds to the averages in equation (5.5) being evaluated at simultaneous times $t = 0$ and similarly for time t. The intermediate scattering function $S(\mathbf{q},t)$ measured is proportional to $\sum_{i,j} < S_i^{\alpha}(0)S_j^{\beta}(t) > e^{-i\mathbf{q}\cdot(\mathbf{r}_i-\mathbf{r}_j)}$. For XPCS, the assumption is often that the Siegert relation holds, i.e. that $g_2(\mathbf{q},t)$ is proportional to $|S(\mathbf{q},t)/S(\mathbf{q},0)|^2$. However, it is not necessary to make this approximation in the present case. The time dependence of the scattering intensity given by equation (5.7) involves two terms: The first term has a time scale of nanoseconds, and the second term yields the slow fluctuation of the EA order parameter, occurring at much longer time scales, which can be probed by XPCS experiments.

Even if it turns out that the EA order parameter shows no dynamics at all in the time scales that we can measure, we can detect its magnitude from the long-time asymptotic form of $(g_2 - 1)$, which will not decay to zero for a non-ergodic system like a spin glass.

5.5 Materials and Methods

The spin glass system we chose is the $Cu_{1-x}Mn_x$ with varying Mn concentrations, which is one of the most well-studied spin glass systems to date[21, 22]. For this system, the spin glass temperature decreases with decreasing Mn concentration[18, 23]. The CuMn was deposited by co-sputtering in Ar atmosphere to avoid the crystallization and to improve the homogeneity. The CuMn film ($\sim$ 300 nm) was grown on a SiN substrate in order to carry out the soft x-ray scattering measurements in transmission geometry and capped by Cr ($\sim$ 5 nm) to prevent oxidation. (Samples were made by Sheena K.K. Patel from Prof. Eric Fullerton's group.)

Coherent x-ray scattering experiments were carried out at beamline 12.0.2.2 of the Advanced Light Source, Lawrence Berkeley National Laboratory. A linearly polarized incident x-ray beam was tuned to the Mn L_3 edge at 636 eV to access the resonant magnetic scattering in transmission geometry. The incident x-ray beam was also tuned to 10 ev below the Mn L_3 edge to get purely charge scattering background. A 5 μm diameter pinhole was put in the beam path to establish transverse coherence of the incident x-ray beam. The pinhole and the sample were mounted on the same stage to avoid any relative motion. The speckle patterns were collected by a charge-coupled device (CCD) area detector, located 0.45 m downstream from the sample. For each measurement, we reduced the temperature from room temperature while monotonically approaching T_g and waited until the temperature was stabilized with 10 mK. The auto-correlation function was calculated by the multi-tau method[24].

5.6 Results and Discussions

In order to make sure that the transition temperature exists in this system and the quality of sample. First, we measured the static susceptibility changing with temperature under ZFC and FC cases. The samples are $Cu_{1-x}Mn_x$ with x as 4%, 8%, 12%, 16%, and 20%. DC susceptibilities of CuMn spin glass versus temperature for 8 atom% and 12 atom% are shown as

Fig 5.1. (Measurements were done by Dr. Sheng Ran from Prof. Brian Maple's group.) The spin glass temperatures of different samples are listed in Table 5.1, which decrease with lowering Mn concentration, and are similar to the values reported in the previous literatures. It is worth noting that $Cu_{80}Mn_{20}$ is very close to the border between spin glass and ferromagnetic phases[25].

Table 5.1: Spin glass temperature changes with various concentrations of Mn in $Cu_{1-x}Mn_x$ spin glasses

% (x) of Mn	spin glass transition temperature (T_g) from DC susceptibility
20	70K
16	60K
12	45K
8	30K
4	20K

XPCS measurements were made mainly on the $Cu_{88}Mn_{12}$ sample. The typical speckle pattern recorded by the CCD is shown in Fig 5.2 . Because the magnetic scattering from the spins is much less than the static charge scattering, it would be visually difficult to see the speckles changing from the different time snapshots. The T_g for this sample is around 45K, so one would expect a large change in the dynamics of the spins to be observed as we approach it. Movies with various frame time resolution and duration were taken based on the measuring temperature for seeing the evolvement of the speckle pattern.

As stated above, the x-ray photon energy was tuned to the Mn L_3 edge (636 eV) at the resonance energy for enhancing the spin scattering, while the off-resonance energy at 10 eV below Mn L_3 edge was used for catching only static charge scattering. From the previous results we have got at Brookhaven National Laboratory (BNL), we can tell that the large **q** region is where magnetic scattering is significant while the small **q** regime is where charge scattering dominates (see Fig 5.3). Since the magnetic scattering is appreciable only at large **q** region, Fig 5.4 shows the $g_2 - 1$ curves averaged from $q = 6.2 \times 10^{-3} \AA^{-1}$ to $q = 6.6 \times 10^{-3} \AA^{-1}$ for 80K at resonance and off-resonance energy. The resonant curve shows the decay associated with magnetic scattering,

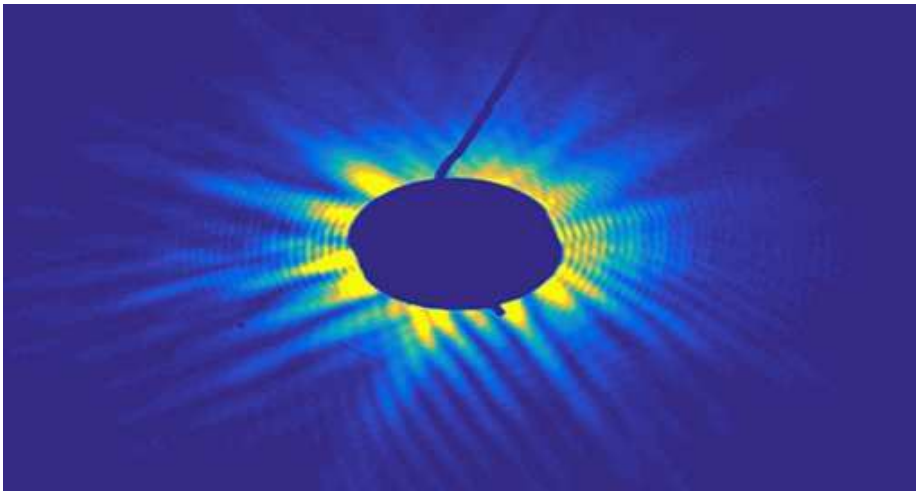

Figure 5.2: Speckle pattern recorded by area CCD detector of $Cu_{88}Mn_{12}$ spin glass sample.

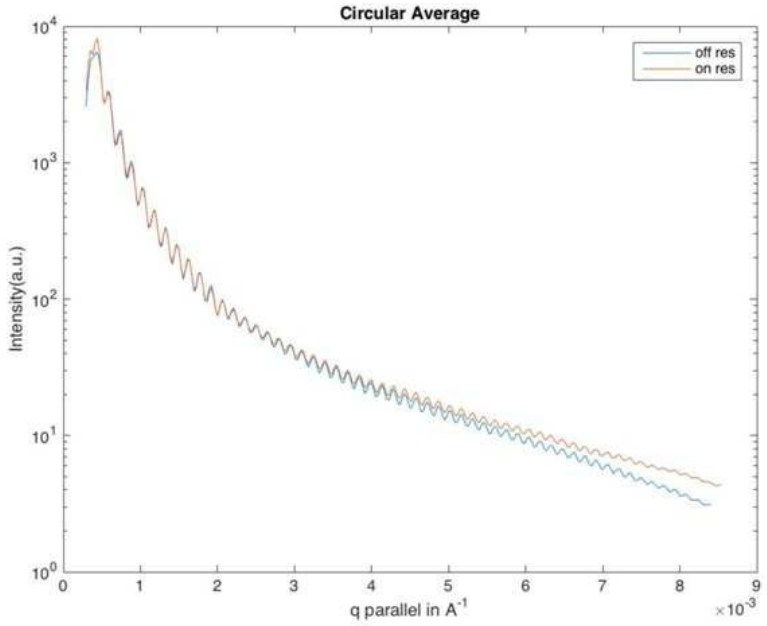

Figure 5.3: Normalized scattering intensity of every pixel at resonance energy and off-resonance energy versus q($\mathring{A}^{-1}$)

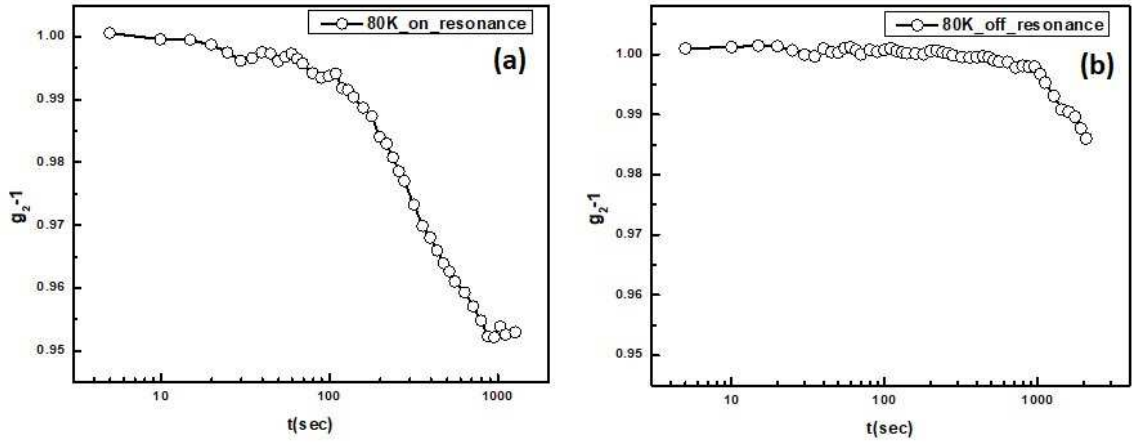

Figure 5.4: $g_2 - 1$ functions for $Cu_{88}Mn_{12}$ spin glass sample at temperature = 80K in (a) resonance and (b) off-resonance energy.

while the off-resonant part has no decay since it is mainly from charge scattering. We know that

$$g_2(\mathbf{q},\tau) = \frac{< I(\mathbf{q},t)I(\mathbf{q},t+\tau) >}{< I(\mathbf{q},t) >^2} \tag{5.9}$$

Substituting equation (5.5) in equation (5.9), we find $g_2(\mathbf{q},\tau)$ constitutes of three terms, two of which involve $\chi(\mathbf{q},\tau)$ and will thus decay rapidly in nanoseconds or faster, and a component which involves the slow fluctuation of EA order parameter. At off-resonance energy, only the static charge scattering can be detected, so there is no dynamics can be seen except for the direct beam decay. Fig 5.5 shows $g_2 - 1$ functions for three different ranges of q at 80K for both the resonance and off-resonance scattering. It can be seen that the resonance scattering at large q shows dynamical fluctuations (as already shown in Fig 5.4), while the scattering at small q values at resonance energy and at all q values at off-resonance energy shows no decay, since it is dominated by charge scattering. At resonance energy, the $g_2 - 1$ curve of the large $\mathbf{q}$ region shows the fast decay and reaches the baseline after the decay. The fast decay is not due to the beam change which we can see from the off-resonance case, since the time scales are different.

If we compare the normalized scattering intensity of every pixel at resonance energy and

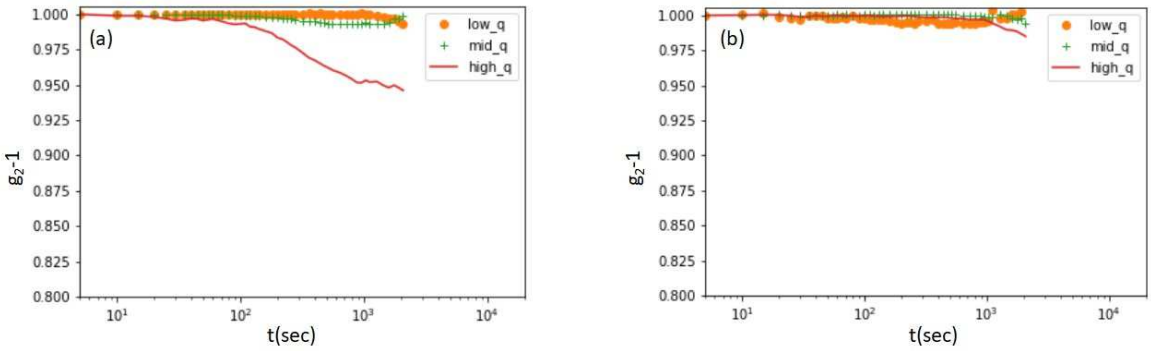

Figure 5.5: $g_2 - 1$ functions for $Cu_{88}Mn_{12}$ spin glass sample at temperature = 80K in (a) resonance and (b) off-resonance energy with various q values. Here: high q=$6.4 \times 10^{-3}\mathring{A}^{-1}$, mid q =$4.0 \times 10^{-3}\mathring{A}^{-1}$, and low q=$1.9 \times 10^{-3}\mathring{A}^{-1}$

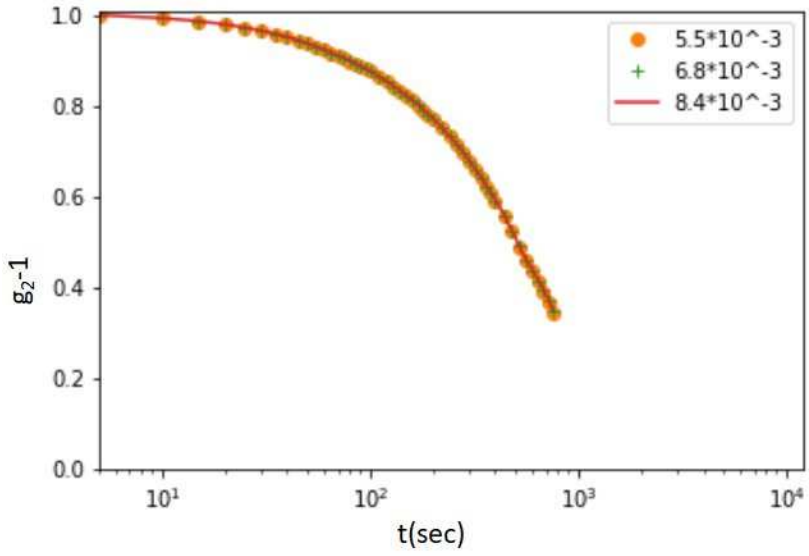

Figure 5.6: Normalized $g_2 - 1$ functions at resonance energy for $Cu_{88}Mn_{12}$ spin glass sample at different q values in magnetic scattering dominating region.

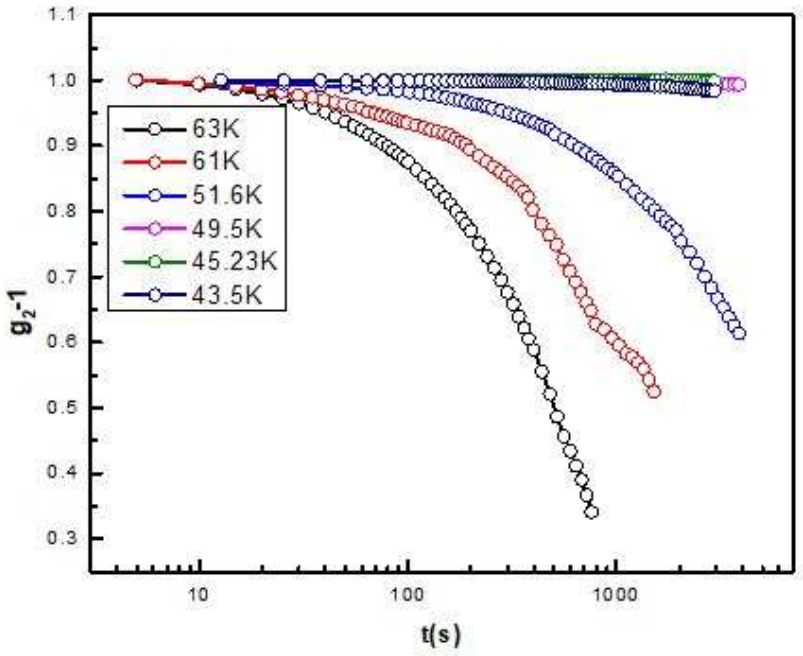

Figure 5.7: Normalized $g_2 - 1$ functions at resonance energy for $Cu_{88}Mn_{12}$ spin glass sample at different temperatures.

off-resonance energy, we can tell the magnetic scattering starts dominating from $q \geq 4 \times 10^{-3} \AA^{-1}$, as shown in Fig 5.3. In this region of $\mathbf{q}$, the normalized $g_2(\mathbf{q}) - 1$ curves overlap each other very well (see Fig 5.6), which means that the fluctuation of the spins are q independent.

The normalized $g_2 - 1$ curves shown in Fig 5.7 show strong temperature dependence. We observe the dynamics are faster at higher temperatures and then slow down as the temperature decreases. For $T < 50K$, the decay constants for $g_2 - 1$ has reached the same time as the incident beam decay, which means we have reached the limit of our time resolution. No decay seen below 45K shows the static EA order parameter which appears below the freezing temperature. Below 70K, the curves can not reach the baseline, because the time scale will be too long to be observed and beyond the instrumental stability. The normalized auto-correlation functions also have been normalized by the g_2 function of direct beam to get rid of the fluctuation of the incident beam.

Fig 5.8 shows one of the $g_2 - 1$ function fitted with the simple exponential decay. In fact, most of the $g_2 - 1$ functions can also be fitted with a pure exponential. The fact, we see the

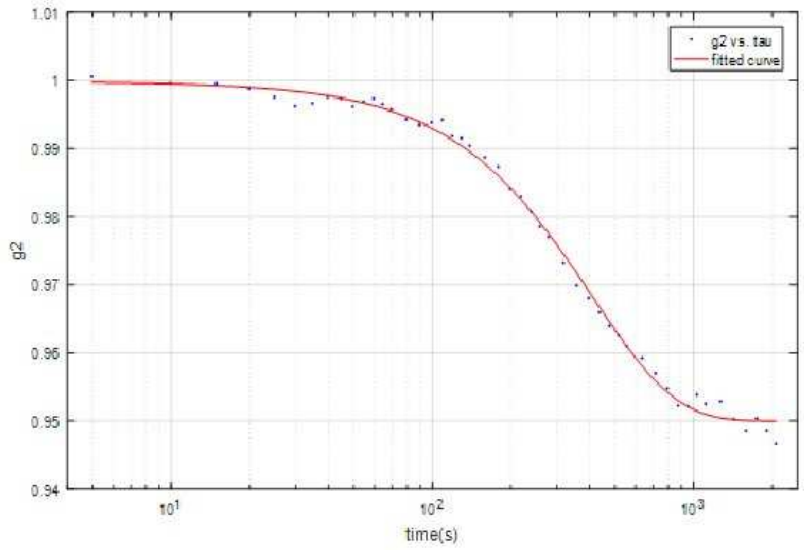

Figure 5.8: Experimental data and fitting curve of $g_2 - 1$ function for $Cu_{88}Mn_{12}$ spin glass sample at resonance energy. Temperature = 80K.

pure exponential of g_2, rather than the stretched or compressed one seen in glassy or jammed systems, implies that we are observing the true dynamical critical behavior for the order parameter fluctuations.

The relaxation time constant can be obtained from the fitted curve as shown in Fig 5.8 for 80 K. In Fig 5.9 we plot the relaxation time constant as a function of temperature and fit the data with the following function

$$\tau(T) = \frac{A}{(T - T_g)^B} \tag{5.10}$$

We obtain a good fit with $T_g = 44.12K$ and $B = 2.682$. From the Fig 5.9, we can observe that τ dramatically increases as $T < 50K$. The transition temperature fitted from equation (5.10) is consistent with the T_g obtained from the DC susceptibility measurement.

If we plot the time averaged intermediate scattering functions $S(\mathbf{q})$ at different temperatures at the resonance energy, we can see $S(\mathbf{q})$ will become $\mathbf{q}$ independent at large $\mathbf{q}$ regime where magnetic scattering dominates.(see Fig 5.10) In the small $\mathbf{q}$ region, $S(\mathbf{q})$ decreases with increasing $\mathbf{q}$ since it is mainly from charge scattering. It is interesting that $S(\mathbf{q})$ increases at low $\mathbf{q}$

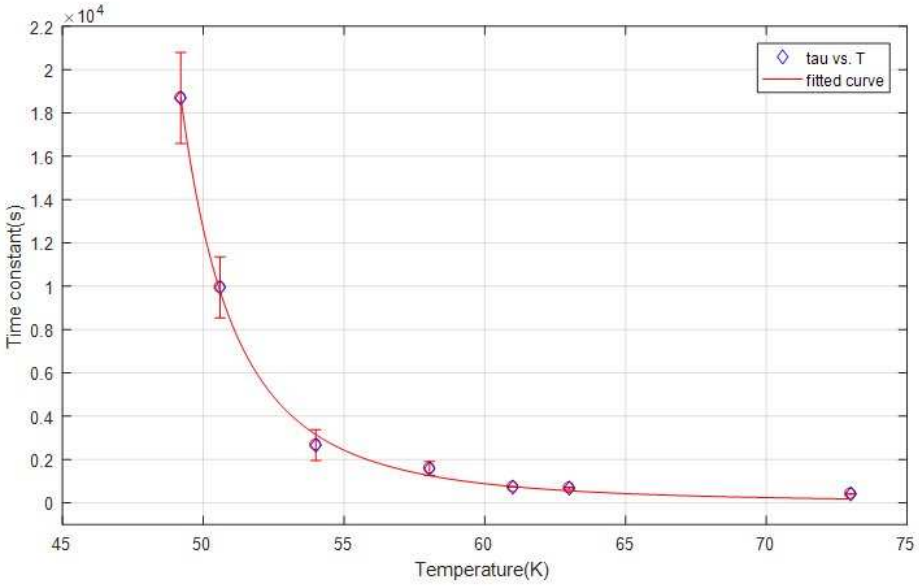

Figure 5.9: Time constant versus temperature for $Cu_{88}Mn_{12}$ spin glass sample(T_g = 45K) .

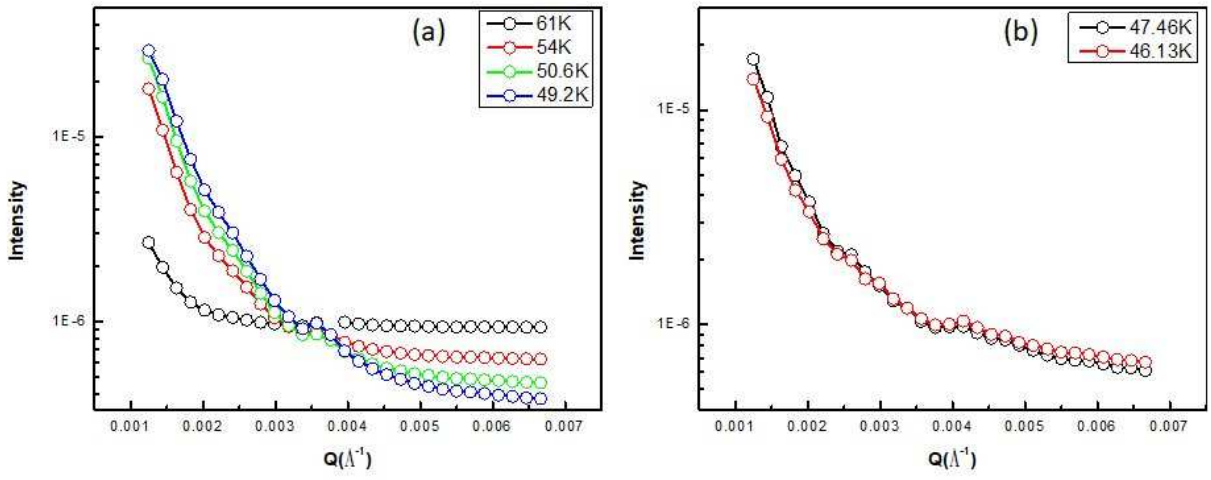

Figure 5.10: Time averaged intermediate scattering functions $S(\mathbf{q})$ at different temperatures at (a) resonance energy and (b) off-resonance energy.

with reducing temperatures, while decreases at large **q**. We speculate this behavior correlated with the enhancement of the magnetic scattering at the low **q** region. At off-resonance energy, $S(\mathbf{q})$ decreases monotonically with increasing **q** and becomes temperature independent, because there is no magnetic scattering contribution.

5.7 Conclusion

We have used XPCS to investigate slow dynamics of the magnetic spins in CuMn spin glasses. The dynamics show a collective behavior due to the long-range RKKY interactions and the auto-correlation functions correlated with the EA order parameter. From the auto-correlation functions, we could observe the fluctuation of EA order parameter directly. Therefore, it is remarkable that we can see the dynamical critical behavior even at 80K, which is almost twice of the value of T_g (45K for $Cu_{88}Mn_{12}$ from DC susceptibility). For a second-order phase transition, this is quite unusual. The relaxation time constant versus temperature indicates the transition temperature exists. Unlike the T_g obtained from AC susceptibility measurements, which are frequency dependent, the T_g obtained from $\tau(T)$ does not change. The EA model considers the spins frozen below the transition temperature, giving a fixed and non-zero EA parameter in the long time scale, and we also see the almost constant g_2 curves when we approach the so-called spin glass transition temperature as we have expected.

The content of this chapter, is an ongoing project with great help from Sujoy Roy in Lawrence Berkeley National Laboratory. The extension of the work is in collaboration with Prof. Brain Maple, Prof. Eric Fullerton, Dr. Sheng Ran, Dr. Rupak Bhattacharya and Sheena K.K. Patel. The dissertation author was the primary investigator and author.

Bibliography

[1] Muneyuki Date and Mitsuhiro Motokawa. Magnetic resonances in the ising spin ferro-and antiferromagnets. *Journal of Applied Physics*, 39(2):820–821, 1968.

[2] DK Finnemore, LJ Williams, FH Spedding, and DC Hopkins. Neutron diffraction and susceptibility study of dilute la-rare-earth alloys. *Physical Review*, 176(2):712, 1968.

[3] D Davidov, JA Mydosh, GJ Nieuwenhuys, and K Baberschke. Coexistence of superconductivity and spin glass magnetic freezing. *Journal of Physics F: Metal Physics*, 7(2):L47, 1977.

[4] Marc Mézard, Giorgio Parisi, and Miguel Virasoro. *Spin glass theory and beyond: An Introduction to the Replica Method and Its Applications*, volume 9. World Scientific Publishing Company, 1987.

[5] David J Thouless, Philip W Anderson, and Robert G Palmer. Solution of'solvable model of a spin glass'. *Philosophical Magazine*, 35(3):593–601, 1977.

[6] Koji Hukushima and Koji Nemoto. Exchange monte carlo method and application to spin glass simulations. *Journal of the Physical Society of Japan*, 65(6):1604–1608, 1996.

[7] H Maletta and W Zinn. Spin glasses. *Handbook on the Physics and chemistry of Rare Earths*, 12:213–356, 1989.

[8] C Kittel. Indirect exchange interactions in metals. In *Solid state physics*, volume 22, pages 1–26. Elsevier, 1969.

[9] KH Fischer. Static properties of spin glasses. *Physical Review Letters*, 34(23):1438, 1975.

[10] V Cannella and JA Mydosh. Magnetic ordering in gold-iron alloys. *Physical Review B*, 6(11):4220, 1972.

[11] J Chalupa. The susceptibilities of spin glasses. *Solid State Communications*, 22(5):315–317, 1977.

[12] Samuel Frederick Edwards and Phil W Anderson. Theory of spin glasses. *Journal of Physics F: Metal Physics*, 5(5):965, 1975.

[13] H Maletta, W Felsch, and JL Tholence. Spin glass behaviour in the non-metallic system (eusr) s. *Journal of Magnetism and Magnetic Materials*, 9(1-3):41–43, 1978.

[14] F Holtzberg, JL Tholence, H Godfrin, and R Tournier. New magnetic properties of a dilute spin-glass. *Journal of Applied Physics*, 50(B3):1717–1719, 1979.

[15] RR Galazka, Shoichi Nagata, and PH Keesom. Paramagneticspin-glassantiferromagnetic phase transitions in cd 1- x mn x te from specific heat and magnetic susceptibility measurements. *Physical Review B*, 22(7):3344, 1980.

[16] Shoichi Nagata, RR Galazka, DP Mullin, H Akbarzadeh, GD Khattak, JK Furdyna, and PH Keesom. Magnetic susceptibility, specific heat, and the spin-glass transition in hg 1- x mn x te. *Physical Review B*, 22(7):3331, 1980.

[17] H Maletta and W Felsch. Insulating spin-glass system eu x sr 1- x s. *Physical review B*, 20(3):1245, 1979.

[18] Shoichi Nagata, PH Keesom, and HR Harrison. Low-dc-field susceptibility of cu mn spin glass. *Physical Review B*, 19(3):1633, 1979.

[19] J Ferré, J Rajchenbach, and H Maletta. Faraday rotation measurements of time dependent magnetic phenomena in insulating spin glasses. *Journal of Applied Physics*, 52(3):1697–1702, 1981.

[20] F Mezei, W Knaak, and B Farago. Neutron spin echo study of dynamic correlations near liquid-glass transition. *Physica Scripta*, 1987(T19B):363, 1987.

[21] L Lundgren, P Svedlindh, P Nordblad, and O Beckman. Dynamics of the relaxation-time spectrum in a cumn spin-glass. *Physical review letters*, 51(10):911, 1983.

[22] Daniel S Fisher and David A Huse. Nonequilibrium dynamics of spin glasses. *Physical Review B*, 38(1):373, 1988.

[23] CAM Mulder, AJ Van Duyneveldt, and JA Mydosh. Susceptibility of the cu mn spin-glass: Frequency and field dependences. *Physical Review B*, 23(3):1384, 1981.

[24] Davide Magatti and Fabio Ferri. Fast multi-tau real-time software correlator for dynamic light scattering. *Applied Optics*, 40(24):4011–4021, 2001.

[25] W Abdul-Razzaq and JS Kouvel. Magnetic phase diagram of disordered ni-mn near the multicritical point. *Physical Review B*, 35(4):1764, 1987.

Chapter 6

Conclusions

In this thesis, we present the studies about structures and dynamics of different systems by using variety of x-ray scattering techniques, including small angle x-ray scattering (SAXS), grazing incident small angle x-ray scattering (GISAXS), and x-ray photon correlation spectroscopy (XPCS). The works are summarized here.

In Chapter 3, we have investigated the three-dimensional ordering structures occurring in the phase separated lipid multilamellar. First, we carried out the GISAXS measurements on the DPPC-DOPC multilayer membranes with various cholesterol concentrations. We thus see that the so-called "'raft-like' domains in these phase separated stacked lipid bilayers. The multilamellar of both phases retained significant amounts of the interlayer water between their head groups, and the periodic multilamellar structure was quite robust in the vacuum. The symmetric side peaks imply that the in-plane ordering exists.To obtain more information about the in-plane structures, we conducted the SAXS experiments and tuned the energy of x-rayed at Carbon K-edge to increase the contrast. The results show the domains are actually hierarchical in structure, with columnar L_o phase sub-domains self-assembling in a local face-centered distorted square lattice and clustering to form domains which are then randomly distributed throughout the membrane. The fact that these ordered structures which also involve adsorbed inter-lamellar water are stable

in high vacuum environments could also lead to novel applications, since many external moieties or functionally treated nanoparticles are known, to preferentially reside in the L_o domains.

In Chapter 4, we have studied the dynamics of a dilute solution of polymer-chain-grafted gold nanoparticles in polymer melts using x-ray photon correlation spectroscopy. We have observed the cross-over of the diffusive behavior of the nanoparticle. When the host matrix polymer chains are below the molecular weight (MW) for entanglement, normal isotropic diffusion of the gold nanoparticles is seen. Anomalous diffusion of the nanoparticles is observed that can be described in terms of ballistic motion and generalized Levy walks, if the host polymer chains have a molecular weight above the entanglement molecular weight. Molecular dynamics simulations of a single gold nanoparticle diffusing in a partially aligned polymer network semiquantitatively reproduce the experimental results to a remarkable degree. The results help to elucidate how nanoparticles can under certain circumstances move rapidly in polymer networks.

Chapter 5 describes the slow dynamics of magnetic spins in the spin glass system. We have used XPCS to investigate the arrangement of the spins in CuMn spin glasses. By the auto-correlation function calculated from the intensity changes of the speckles, we can know the information on the spin dynamics. The dynamics show a collective behavior due to the long range RKKY interactions and the auto-correlation functions correlated with the EA order parameter. The relaxation time constant versus temperature indicates the transition temperature exists. From the auto-correlation function, we could observe the fluctuation of EA order parameter directly, and we also see the almost constant g_2 curves when we approach the so-called spin glass transition temperature as we have expected.